Physics of the Earth and Planetary Interiors 321 (2021) 106707

Contents lists available at ScienceDirect

Physics of the Earth and Planetary Interiors

journal homepage: www.elsevier.com/locate/pepi

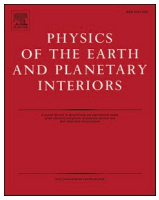

Frequency-size distributions of Wadati-Benioff zone and near-boundary intraplate earthquakes: Implications for intermediate and deep seismicity

Jordan P. Todes [a,1], Emile A. Okal [a,*], Stephen H. Kirby [b]

[a] Department of Earth and Planetary Sciences, Northwestern University, Evanston, IL 60208, USA
[b] United States Geological Survey, 345 Middlefield Road, Menlo Park, CA 94025, USA

ARTICLE INFO

Keywords:
Subduction zones
Frequency-size relations
Intraplate earthquakes

ABSTRACT

We conduct a systematic analysis of the frequency-moment distribution of earthquake populations in Wadati-Benioff zones, motivated by a three-fold increase in the available GlobalCMT database since the previous study by Okal and Kirby (1995), in which some datasets may have been undersampled. We use 100-km depths bins, processed with both least-squares and maximum-likelihood algorithms, and apply an *F*-test methodology to assess the robustness of our results, in particular regarding multi-segment behavior within individual depth bins. Our results generally support Okal and Kirby's (1995), and the new enlarged dataset suggests the resolution of the third segment predicted by these authors for the 500–600 km bin in Tonga, in the framework of their three-tier model for two-step source saturation of seismicity generated by transformational faulting within a wedge of metastable olivine. In the 200–300 and 300–400 km depth bins, we find comparable behaviors, revealing the artificial nature of the traditional 300-km boundary between "intermediate" and "deep" earthquakes. Our view is that it may be deeper than 300 km, and fundamentally variable between distinct subduction zones.

We extend our study by considering frequency-moment distributions for intraplate earthquakes in oceanic lithosphere before it subducts at trenches. Those results support the interpretation of seismicity in the shallowest portions of slabs as involving the reactivation of existing faults under a process of dehydration embrittlement. However, outer rise events occurring immediately before subduction feature different population statistics, which are probably related to the release of bending stresses of a different origin.

1. Introduction

The purpose of this paper is to re-assess variations in frequency-size distributions for a number of global, regional, and depth-dependent datasets of earthquakes, primarily in Wadati-Benioff zones (WBZs). We are motivated by the fact that previous studies, several dating back at least 20 years (*e.g.*, Giardini, 1988; Pacheco et al., 1992; Frohlich and Davis, 1993; Wiens et al., 1994; Okal and Kirby, 1995), suffered from undersampling of the seismic record, in particular with regard to large and deep earthquakes or when restricted to specific regional datasets. In addition, we explore the potential implications, for intermediate depth seismicity, of the frequency-moment distribution in the outer-rise region of subduction zone trenches, as well as frequency-moment distributions of mid-ocean ridge and oceanic intraplate earthquake populations. We ultimately support the main findings of Okal and Kirby (1995), although their frequency-moment distributions for deep earthquakes (< 500 km) could clearly have suffered from under-representation in the then available seismic record. Their hypothesized framework for a three-regime behavior of frequency-size relationships in deep earthquakes, driven by seismogenic zone saturation, is also supported by our results in the Tonga subduction zone. This model stands in contrast to the dual-mechanism hypothesis recently proposed by Zhan (2017, 2020), also based on a frequency-magnitude distribution study. Finally, it is suggested that the broad similarity of Gutenberg-Richter relations in the global populations of intraplate oceanic and intermediate-depth earthquakes reflects the occurrence of the latter on reactivated subducted faults, potentially driven by mineral dehydration along the subducting slab (Okazaki and Hirth, 2016).

Global seismology has traditionally been fueled by two opposite, but complementary, approaches. On the one hand, a sense of homogeneity of the planet has allowed the development of global velocity models as early as 1907, as well as the observation of the uniformity of shallow and

* Corresponding author.
E-mail address: emile@earth.northwestern.edu (E.A. Okal).
[1] Present Address: Department of the Geophysical Sciences, University of Chicago, Chicago, IL 60637, USA.

https://doi.org/10.1016/j.pepi.2021.106707
Received 26 September 2020; Received in revised form 27 March 2021; Accepted 29 March 2021
Available online 10 June 2021

deep seismic sources, already referred to as a "consanguinity" by Leith and Sharpe (1936). On the other hand, more detailed, second order analyses have later pointed out significant lateral heterogenities, as documented, for example, by the field of seismic tomography, developed since the 1980s. The study of frequency-size distributions has been no exception to this duality of approaches, encompassing both investigations on a global scale and studies exploring (and seeking to contrast) the behavior of individual datasets of regional events in various tectonic environments. As discussed below, the homogeneous dataset of GlobalCMT solutions selected in the present study remains limited in size, to the extent that a full separation as a function of both depth and geographical regions often results in populations too small to conduct meaningful frequency-size investigations. In this context, our approach in the present paper will be closer to a global one, designed to investigate general features of the distribution of earthquakes as a function of the first-order history of the slab during the subduction process, namely the increase in depth, rather than any possible differences expressing lateral, more detailed deviations. This approach can be regarded as complementary to one emphasizing lateral heterogeneity at the cost of a coarser depth sampling (*e.g.*, Zhan, 2017).

2. Background

It has long been noted that small earthquakes are, simply put, more frequent than larger ones. Following the empirical introduction of seismic magnitude by Richter (1935), which broadly speaking scaled earthquake sources in a frequency band corresponding to perceived shaking, Gutenberg and Richter (1941) introduced their landmark "rule of tenfold increase". Subsequently, this behavior was formally modeled through the relation

$$\log_{10} N = a - bM \tag{1}$$

in which M is a particular value of magnitude, and N is the number of earthquakes in a particular dataset with a magnitude equal to or greater than M (Gutenberg and Richter, 1949). The absolute value of the slope of the regression in Eq. (1), referred to as the b-value of an earthquake population, has been found to be reasonably invariant from 1 for numerous large datasets of shallow tectonic earthquakes. It is only when seismicity arises as aftershocks or from a non-tectonic source (for instance, from volcanic activity or processes such as hydraulic fracking) that b-values deviate significantly from 1 (Utsu, 1966; Minakami, 1974; Frohlich and Davis, 1993; Tafti et al., 2013). As such, b-value observations have been used to identify volcanic swarms, and have potential for distinguishing seismic swarms triggered by hydraulic fracking from ambient seismicity.

Upon adoption of the seismic moment M_0 as the standard physical quantification of earthquake size, an analogous frequency-moment relation was proposed by Molnar (1979):

$$\log_{10} N = \alpha - \beta \log_{10} M_0 \tag{2}$$

As thoroughly reviewed by Okal and Romanowicz (1994), the relationship between the b- and β-values of a given population of earthquakes depends on the variation of any given seismic magnitude scale (*e.g.*, m_b, M_s) with seismic moment M_0, which in turn is affected by the saturation of these magnitude scales as earthquake size grows (Kanamori and Anderson, 1975; Geller, 1976). In particular, Okal and Romanowicz (1994) concluded that the fact that a b-value of 1 is widely reported stems from the use of heterogeneous magnitude catalogues (m_b for smaller earthquakes, M_s for larger ones), which can lead to biased physical interpretation of the properties of the relevant seismogenic zones. It is therefore crucial that the seismic moment M_0, calculated in a uniform, consistent manner within a given catalogue, be employed for investigation of the frequency-size relationship in earthquake populations of sufficient size and magnitude.

A substantial amount of literature has been devoted to the understanding of frequency-size distributions: see, *e.g.*, Båth (1981), Frohlich and Davis (1993) and Utsu (1999) for thorough reviews. From a theoretical perspective, a landmark contribution was Rundle (1989), who proposed a three-step argument to justify a b-value of unity for shallow earthquakes. Because it was built on various assumptions which may break down for intermediate or deep ones, we review his derivation in some detail. First, the process of faulting is assumed to be scale-invariant, so that the frequency of earthquakes of a given size is inversely proportional to the fraction of seismogenic domain involved ("any seismogenic material stands the same chance of being released by a small or large event"); as a result, the number $n(M_0)$ of earthquakes with moment M_0 scales with linear size L as $n \propto L^{-D}$, where D is the fractal dimension of the seismogenic zone. Second, scaling laws predict that the linear dimension L of an earthquake has a power-law dependence on $M_0 : L \propto M_0^{\lambda}$. Third, the magnitude used, M, scales with the logarithm of the seismic moment M_0 with a factor μ:

$$M = \mu \log_{10} M_0 + m \tag{3}$$

As a result, $n(M_0)$ (and its integral $N(M_0)$ by virtue of the properties of the exponential function) will scale as $M_0^{-\beta}$ with $\beta = D\lambda$, or follow (1) with $b = \beta/\mu = D\lambda/\mu$.

For shallow earthquakes, the vast majority of seismogenic domains have $D = 2$ ("earthquakes take place on [two-dimensional] faults"), and in the absence of saturation, $\lambda = 1/3$ (Kanamori and Anderson, 1975). One then predicts $\beta = 2/3$. As for μ in (3), seismological practice has enshrined a value of 2/3 (Kanamori, 1977), leading to $b = 1$, as originally observed by Gutenberg and Richter (1949). Note, however, that $\mu = 2/3$ corresponds to a range of earthquake sizes where saturation starts to become relevant (Geller, 1976), and may therefore be incompatible with $\lambda = 1/3$ (Okal and Romanowicz, 1994). In this context, this paper will use exclusively the parameter β defined by (2).

Rundle's (1989) derivation lends itself to some level of adaptation when its underlying assumptions are violated. Such would be the case, for example, of three-dimensional seismogenic zones ($D = 3$). However, the concept of simple scaling laws would require integer values (2, 3, or conceivably 1) for the fractal dimension D and inverse integers (1/3, 1/2 or 1) for λ. The resulting β value would then be expected to take only a limited sample of fractional values, all of which would be in principle possible, albeit not identically probable: 3, 2, 3/2, 1, 2/3, 1/2 and 1/3. Other values would represent inhomogeneous datasets.

Also, the concept of scaling laws is based on the assumption of invariant intensive variables, for example the strain ϵ (or equivalently, stress $\Delta\sigma$) released during the earthquake, which was taken as constant in Rundle's (1989) derivation. Recent advances in source tomography have documented large heterogeneities in slip along fault planes, a dramatic example being the extreme slip on the shallow part of the 2011 Tohoku rupture (Lay et al., 2011), which clearly invalidates the assumption of invariance, at least in the case of such exceptional events.

For shallow earthquakes with comparatively moderate moments, the predicted value, $\beta = 2/3$, is well-documented and upheld in extensive catalogues of moderately large earthquakes (*e.g.*, Kagan, 2002). At larger moments, a sharp increase in β is observed in global and most regional populations beyond a critical "elbow" moment M_c, which can be attributed to the saturation of the fault width W and concurrent limitation of the fault slip Δu under Scholz' (1982) so-called "W model", with a predicted value of $\beta = 1$ at larger moments (Pacheco et al., 1992; Romanowicz and Rundle, 1993). Fig. 1 updates Okal and Romanowicz' (1994) study to a much larger dataset of more than 46,000 earthquakes. Note that the slope of the first segment fits perfectly (to two significant digits) the predicted $\beta = 2/3$, and that of the second one ($\beta = 0.89$) is slightly deficient with respect to the value ($\beta = 1$) predicted under the W-model, while that slope was excessive ($\beta = 1.31$) in the previous study. This simply reflects the absence of truly large earthquakes ($M_0 \geq 5 \times 10^{28}$ dyn*cm) during the early years of the GlobalCMT project, and their probable excess (with respect to an average over longer

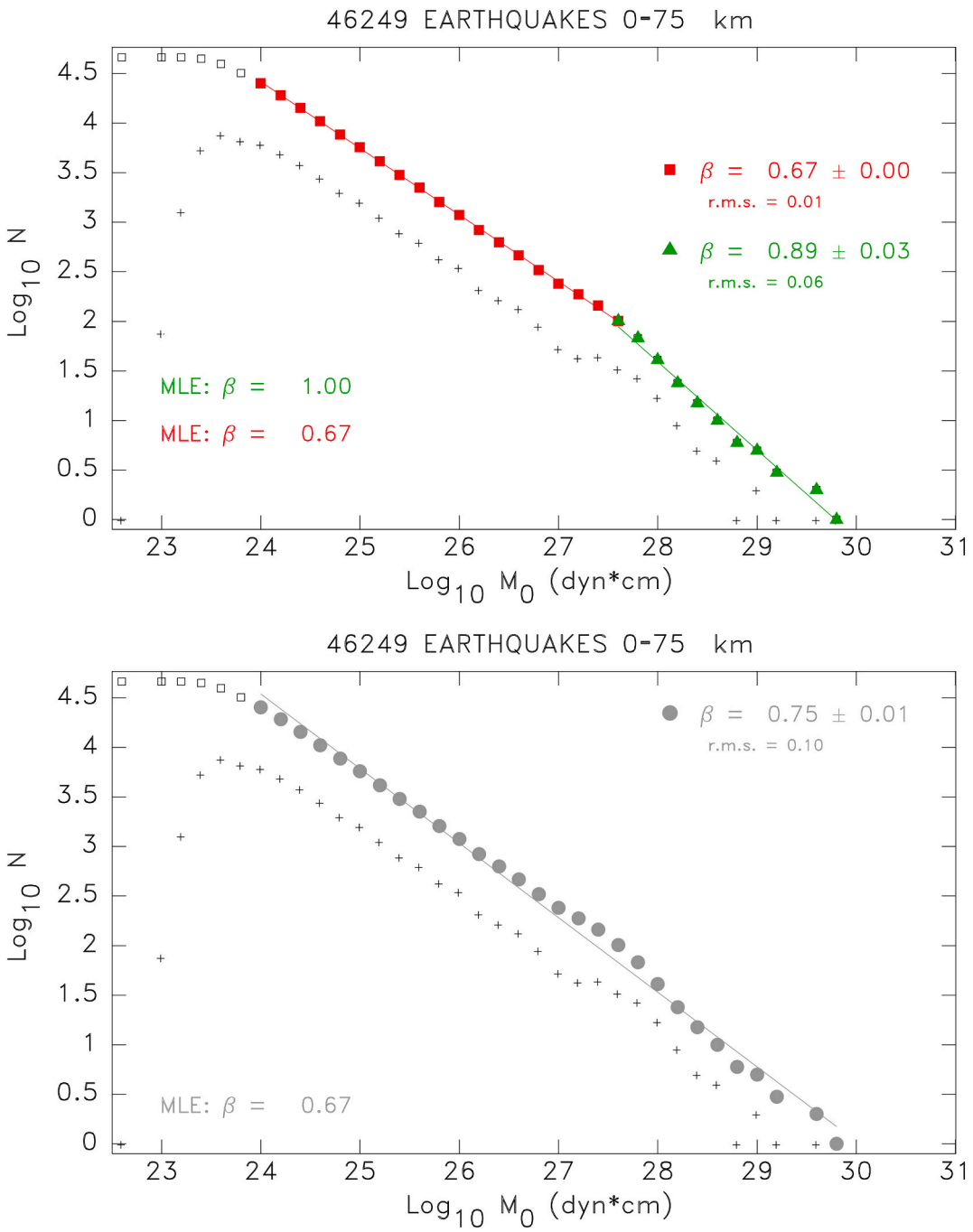

Fig. 1. β-value investigation of dataset of shallow (0–75 km) CMT solutions, updated from Okal and Romanowicz (1994). *Top:* Two-segment regression; *Bottom:* Single segment regression. In each case, the small + signs denote the populations n of the individual bins, the larger symbols the cumulative populations N. The solid symbols show the bins used in the regression, the open ones those ignored on account of incompleteness at lower magnitudes. Results of both the LSQ (upper right) and MLE (lower left) algorithms are listed for each group.

time windows) in the past decades (Sumatra, 2004; Nias, 2005; Chile, 2010; Tohoku, 2011, etc.), resulting in large fluctuations of small numbers at large moments.

More complex frequency-size behaviors would be expected in the case of three-dimensional seismogenic zones ($D = 3$), or in the presence of brecciated material limiting the size of faults and leading to $\lambda > 1/3$; these situations would apply, for example, to volcanic earthquake swarms for which b-values greater than 1 have long been documented (McNutt, 2005). By analogy, and having observed significant departures from Rundle's (1989) paradigm, Okal and Kirby (1995) inferred that the seismogenic zone in subducting slabs may be three-dimensional ($D = 3$), and proposed a two-stage, progressive saturation model in which both transverse dimensions (width and depth) saturate, followed by saturation of the slip Δu, which in Scholz' (1982) framework amounted to a transition from an L-model to a W-model of saturation. Under Okal and Kirby's (1995) model, it was anticipated that the resultant frequency-moment relations would then exhibit a three-tier behavior, and preliminary results were found to that effect (their Fig. 7). This proposition was countered by Zhan (2017), who argued for an alternative hypothesis in which the fractal dimension of earthquake rupture decreases from $D = 2$ to $D = 1$ as the thickness of the metastable olivine wedge in the subducting slab (in which transformational faulting is inferred to occur)

decreases to a minimal value, then increases back to $D = 2$ as alternative seismogenic processes (*e.g.*, dynamic shear banding or shear melting) start to prevail. An additional complexity is the apparently regular occurrence of massive deep earthquakes (*e.g*, Bolivia, 1994; Okhotsk Sea, 2013) which may not adhere to Rundle's (1989) scale-invariance principle (Lundgren and Giardini, 1994).

At intermediate depths (75 to 400 km), we presently lack a satisfactory framework to understand seismogenesis, even though dehydration embrittlement is generally assumed to be an important agent (*e.g.*, Meade and Jeanloz, 1991; Boneh et al., 2019). This is in part due to the generally lesser level of seismicity, which exacerbates the question of undersampling in the catalogues used by previous studies.

In this context, an update to further unravel the nature of Gutenberg-Richter distributions in intermediate and deep-focus earthquake populations is desirable, in order to systematically investigate the robustness of prior studies, and examine geographic heterogeneity in Gutenberg-Richter distributions across subduction zones: this constitutes the primary focus of the present study. We also examine the physical mechanisms driving intermediate depth seismicity in subduction zones, using normal faulting, intraplate earthquake populations within the outer-rise region of subduction trenches as an analog. We are motivated by the possibility that intermediate-depth earthquakes could be triggered by dehydration embrittlement along reactivated faults in the subducting lithosphere (Savage, 1969; Meade and Jeanloz, 1991; Peacock, 2001). In such a framework, the characteristics of fault zones, including their spatial dimensions, would be inherited from those of shallow intraplate seismicity of the oceanic lithosphere, notably in the outer-rise region, leading to comparable earthquake populations and Gutenberg-Richter distributions. Finally, we include in the present study an investigation of near-boundary frequency-size relations in the vicinity of mid-oceanic ridges, and interpret them in the context of physical rupture mechanisms.

3. Methodology

3.1. Database

The dataset used in this study is the Global (formally Harvard) Centroid Moment Tensor catalogue (Dziewonski et al., 1981; Ekström et al., 2012), which contains a systematic, consistent record of earthquake source parameters and moments from 1977 to September 2020. It is acknowledged that this catalogue has a relatively high threshold for inclusion and completeness (in practice, $M_0 = 10^{24}$ dyn*cm),and that, due to its youth (presently 44 years), very large earthquakes may be under- (or possibly over-) represented relative to actual historical trends. An additional problem of the GlobalCMT catalogue is that it can significantly underestimate the largest events; for example, it lists the 2004 Sumatra earthquake at only 3.95×10^{29} dyn*cm, about three times less than determined from the modeling of the Earth's gravest normal modes (Stein and Okal, 2005, 2007; Tsai et al., 2005), in the process making it smaller than the 2011 Tohoku earthquake. However, it is the only catalogue that contains source parameters based on homogeneous measurements and a common inversion algorithm; furthermore, it allows direct comparison to the previous study by Okal and Kirby (1995).

Finally, we did not attempt to "de-cluster" the dataset by removing aftershocks, as suggested originally in Southern California by Gardner and Knopoff (1974). Our choice reflects the general scarcity of aftershocks for deep events, and, when they are present, their more irregular occurrence than for shallow earthquakes (Frohlich, 1987; Kirby et al., 1996b). An additional difficulty is the separation of true aftershocks (defined as occurring on the same fault as the mainshock) from events triggered by stress transfer on a different system of faults (*e.g.*, Freed, 2005), which is exacerbated for non-shallow earthquakes, given the often poorly defined system of faults hosting the main event.

3.2. Computation of β values

There are essentially two algorithms for the computation of b- or β-values. The classical one, used by most early investigators including Okal and Kirby (1995), consists of sorting earthquakes into bins of equal width in units of magnitude (or log of moment), and fitting a straight line of the type (1) or (2) through the cumulative populations of the bins using a least-square (LSQ) regression. The use of cumulative populations is preferred as they represent an integral of those of the individual bins, and as such, offer a smoothing effect against any irregularity in population caused by the combination of finite bin width and undersampling at large sizes.

Another approach consists of computing a "Maximum Likelihood Estimate" (MLE) of b (or β) by noting (Aki, 1965) that for a distribution of the form

$$\log_{10} n(M) = a' - bM \tag{4}$$

the average magnitude of a population with a minimum magnitude M_{min} is given by

$$< M >= M_{min} + \frac{\log_{10} e}{b} \quad \text{or conversely,} \qquad b = \frac{0.434}{< M > - M_{min}} \tag{5}$$

or in terms of moments,

$$< \log_{10} M_0 >= \log_{10} M_0^{min} + \frac{\log_{10} e}{\beta} \quad \text{or conversely,} \qquad \beta = \frac{0.434}{< \log_{10} M_0 > - \log_{10} M_0^{min}} \tag{6}$$

This approach has several advantages, including the extreme simplicity of the computation and its being, at least in principle, insensitive to the details of the binning procedure. For this reason, the MLE algorithm has often been preferred in more recent investigations (*e.g.*, Roberts et al., 2015).

However, both methods suffer from limitations under practical conditions. First, the identity of behavior between n and its integral N is true only when the upper bound of the integral is extended to infinity, which is impossible to achieve in practice on account of (i) the physical limitation to the size of earthquakes stemming from that of fault dimensions, itself limited *a priori* by the finite size of the Earth; (ii) the undersampling of large events in any catalogue of finite duration; and (iii) notwithstanding the above limitations, the impossibility of carrying out numerically an integral extending to infinity. This will affect the fitting of the cumulative population of bins under the LSQ algorithm, which is then expected to exhibit curvature when approaching the maximum observed magnitude, whether the latter is limited physically (i) or empirically (ii). This effect was already noticed by Gutenberg and Richter (1949), but that observation could have been affected by their use of saturating magnitude scales (Okal and Romanowicz, 1994). As a consequence, several modified versions of (1) or (2) have been proposed, *e.g.*, by Ward (1994) and Kagan (2002).

Allowing for a maximum event size M_{max} or M_0^{max}, Eqs. (1) and (2) can be replaced by:

$$\log_{10} N = a - bM + \log_{10}\left[1 - 10^{-b(M_{max} - M)}\right] \tag{7}$$

and

$$\log_{10} N = a - \beta \log_{10} M_0 + \log_{10}\left[1 - \left(M_0 / M_0^{max}\right)^{\beta}\right] \tag{8}$$

In principle, they can be solved numerically for a best-fitting value of b or β. However, a tapered or "maxed" distribution such as given by (8) produces continuous curvature in the distribution, rather than the clear sharp elbow evidenced for shallow earthquakes on Figs. 1 and 2. We

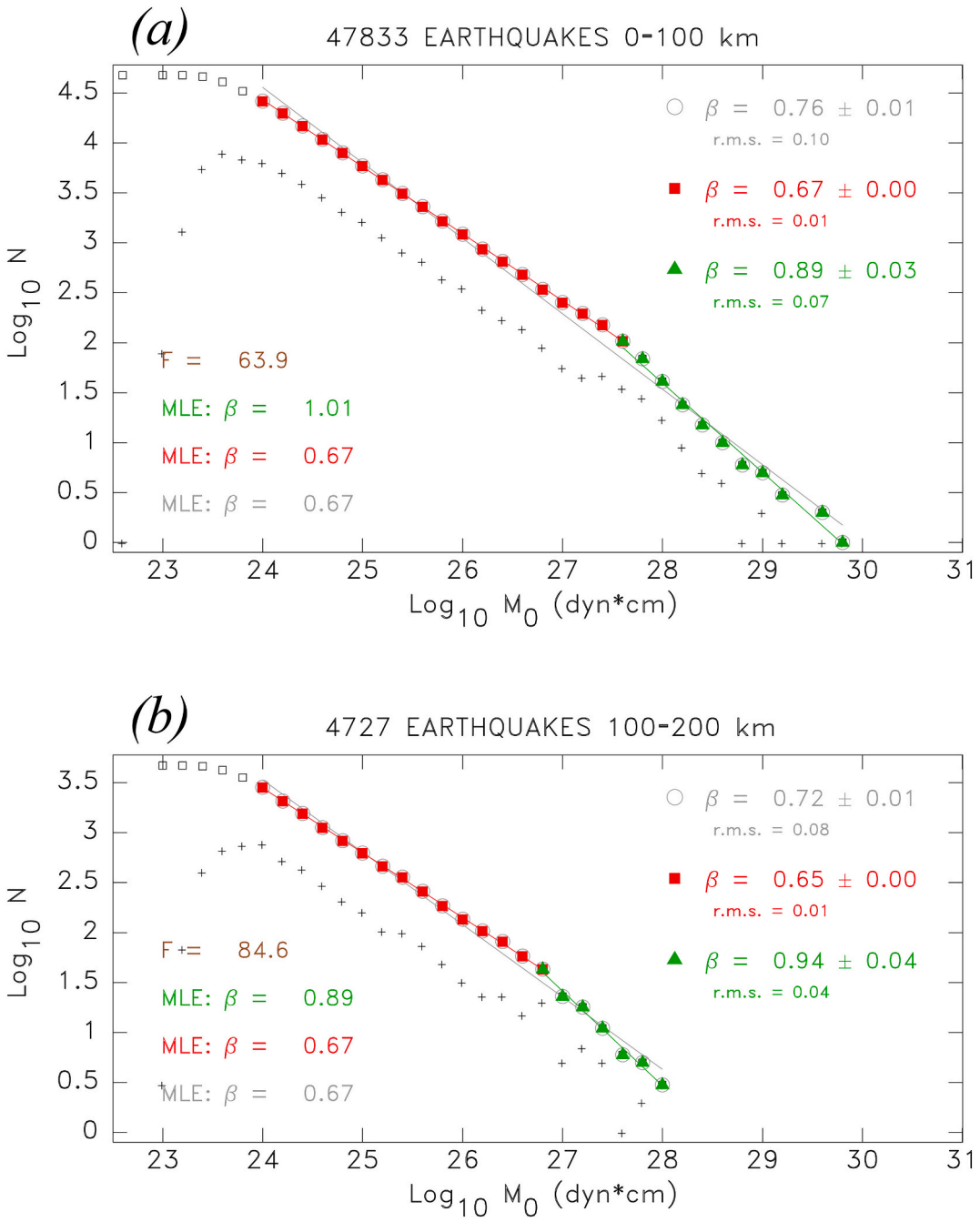

Fig. 2. β-value results for the 0–100 km *(a)* and 100–200 km *(b)* depth bins. The conventions are as in Fig. 1, with the results of a single regression given in light gray, and those of the two-segment regression in red and green. In addition the *F*-test result for one- and two-segment regressions is also given.

have verified that in the seven depth bins described in Section 4, the use of (8) as opposed to a two-segment straight LSQ algorithm does not improve the fit to the cumulative population datasets, and for the two shallowest ones (0–100 and 100–200 km), it significantly degrades it. This is probably due to irregular (under- or over-) sampling at large moments, over a limited time window not representative of the true level of seismicity averaged over geological time intervals.

Similarly, the derivation of Eqs. (5) and (6) assumes that the average magnitude is taken over a population extending to infinite size, and corrections must also be effected in this respect. In a detailed compilation of systematic problems affecting *b*-value determinations, notably for volcanoseismic systems, Roberts et al. (2015) have argued that this effect is generally negligible, but the sample windows which they considered usually extended over several magnitude units, which may not be the case when the population is multi-segmented, as discussed next.

Indeed, the two methods behave differently if the population consists of two segments with different slopes, as detailed here. When the dataset on Fig. 1 is modeled as two segments, the LSQ method yields β-values of 0.67 (undistinguishable from 2/3) for the first segment, and 0.89 for the second one, approaching in the presence of very small numbers of very large earthquakes the value of 1 predicted by Scholz' (1982) *W* model. When modeled as two segments, the MLE algorithm yields slopes of 0.67 and 0.99, perfectly representative of the predicted values.

However, if the population is modeled as a single segment, the LSQ method will yield a β-value intermediate between the two slopes (in this case 0.75). The fact that this is not one of the expectable values under Rundle's (1989) theory is in itself an indicator that the model of a single

regression may not be appropriate. On the other hand, the MLE method will give a result equivalent to the slope at low event sizes (0.67), suggesting a perfect fit to the case $D = 2$; $\lambda = 1/3$. This is because the computation of a mean by the MLE algorithm weights all *events* equally and is therefore relatively insensitive to a scarcer population of very large earthquakes beyond a change in distribution (only 0.6% of the events considered belong to the second segment). By contrast, the LSQ algorithm weights all *bins* equally, with 38% of the bins belonging to the second segment. In this respect, the MLE method is much less efficient at detecting a change in distribution, especially when the latter takes place at large magnitudes. We have also verified this result on synthetic distributions.

On the other hand, the MLE algorithm is less sensitive to fluctuations in small populations of large earthquakes. For example and as discussed above, the second segment of the shallow earthquake population shown on Fig. 1 was regressed differently by LSQ in Okal and Romanowicz (1994) and in the present study using a larger dataset; however, the MLE slope (0.99), largely insensitive to those fluctuations in small populations provides a nearly perfect fit to the value ($\beta = 1$) expected for the second segment under Scholz' (1982) *W*-model.

An additional, serious problem is the resolution of *b*- or β-values by the MLE algorithm, and in particular the robustness of its results, notably when dealing with narrow windows of sampled magnitudes. As detailed in Appendix A, the resulting slopes can be very sensitive to slight fluctuations in the computed value of $<M>$, which can result from the rounding of magnitude values, which constitutes *de facto* binning. This casts additional limitations on the use of the MLE method. We conclude that it cannot be trusted to resolve *b*- or β-values to better than 0.25 units for small datasets, even when the relevant populations span two or more units of magnitude.

These limitations notwithstanding, both the LSQ and MLE methods will be used on all datasets considered in this study, the latter to allow a comparison with other studies which used it exclusively. Formal values of standard deviations for the MLE slopes will be computed using the algorithm of Shi and Bolt (1982), but they can be deceptively small as mentioned above.

3.3. *F*-tests

Many of our results illustrate the presence of a change in the frequency-size distribution for a critical value of the seismic moment, M_c, leading to a two- (or multiple-) segment interpretation. In order to ascertain the robustness of this behavior, we run for each of these cases a so-called "*F*-test", which simply quantifies the probability that any improvement in the quality of fit under an increase in the dimension of the parameter space is due to the actual existence of an additional dimension in the physical problem, rather than to the purely random effect of increasing the parameter space. We refer to Dixon and Massey (1969) for a description of the *F*-test, to Stein and Gordon (1984) for an example of application in a geophysical context, and to Abramowitz and Stegun (1964) for computational aspects. The concept can be illustrated by considering the shallow earthquakes studied in Fig. 1: the *F*-test between the one- and two-segment regressions is $F = 62.4$, about one order of magnitude larger than required ($F_{99} = 6.53$) for confidence at the 99% level (Dixon and Massey, 1969, Table 1); on Okal and Romanowicz' (1994) dataset, lacking the probably over-represented very large events of the 2000s, and thus featuring a steeper second segment, it even rises to $F = 215$ (with $F_{99} = 7.09$). Based on these numbers, it is undisputable that Fig. 1 confirms a change in behavior in the distribution of seismicity around $\log_{10} M_0 = 27.6$.

F-tests will be performed in all relevant cases examined in this paper. In particular, they will be used to quantitatively assert the presence of elbows in the distribution, whose description by Okal and Kirby (1995) was qualified as "not statistically convincing" by Zhan (2017).

4. Results: subduction zones

4.1. The global CMT catalogue as a function of depth

Following the approach of Okal and Kirby (1995), we first consider the variations in frequency-moment relationships that occur in arbitrary bins of 100 km depth for the centroid tensors, as reported in the global CMT catalogue (Dziewonski et al., 1981; Ekström et al., 2012). The resulting regressions are summarized below, listed in Table 1, and compared with the results of Okal and Kirby (1995).

Table 1
Summary of global results obtained in this study.

Depth bin(km)	Number of events	β (LSQ)						β (MLE)			Figure
		All	$M_0 < M_c$	$M_0 > M_c$	$\log_{10} M_c$ (dyn*cm)	*F*Test	F_{99} (†: F_{90})	All	$M_0 < M_c$	$M_0 > M_c$	
Global Shallow Dataset											
0-75[a]	8015	0.79	0.70	1.31	27.2	215	7.09	0.63 ± 0.01	0.63 ± 0.01	1.10 ± 0.13	
0-75[b]	46249	0.75	0.67	0.89	27.6	62.4	6.53	0.67 ± 0.00	0.67 ± 0.00	1.00 ± 0.10	1
0-100[c]	8408	0.79	0.70	1.30	27.6	98.2	6.98	0.59 ± 0.01	0.58 ± 0.01	1.53 ± 0.33	
0-100[d]	47833	0.75	0.67	0.89	27.6	63.9	6.53	0.67 ± 0.00	0.67 ± 0.00	1.01 ± 0.10	2*a*
Wadati-Benioff Zones											
100-200	4727	0.72	0.65	0.94	26.8	84.6	7.21	0.67 ± 0.01	0.67 ± 0.01	0.81 ± 0.09	2*b*
200-300	1073	0.65	0.59	0.66	25.8	19.6	7.91	0.61 ± 0.02	0.61 ± 0.02	0.57 ± 0.05	4*a*
300-400	366	0.63	0.64	0.68	26.0	0.55	2.83†	0.67 ± 0.04	0.70 ± 0.03	0.27 ± 0.01	4*b*
400-500	372	0.64	0.53	0.81	25.8	12.5	7.91	0.54 ± 0.03	0.54 ± 0.02	0.47 ± 0.04	5*a*
500-600	1026	0.72	0.59	0.99	26.2	38.6	7.35	0.65 ± 0.02	0.68 ± 0.02	0.82 ± 0.09	6*a*
>600	586	0.56	0.53	0.71	27.0	9.48	6.98	0.59 ± 0.03	0.61 ± 0.02	0.69 ± 0.14	6*b*
comb'd 200-400	1439	0.65	0.60	0.67	25.6	15.4	7.91	0.63 ± 0.02	0.65 ± 0.01	0.49 ± 0.03	
Separate Tonga											
400-500 Tonga	151	0.72	0.71	1.20	26.4	3.61	2.93†	0.73 ± 0.06	0.78 ± 0.07	2.19 ± 1.28	5*b*
400-500 Non-T	221	0.59	0.50	0.68	26.2	8.40	7.91	0.44 ± 0.02	0.46 ± 0.02	0.29 ± 0.02	5*c*
500-600 Tonga	707	0.79	0.83	0.73	25.3	34.7	7.91	0.82 ± 0.03	0.81 ± 0.02	0.67 ± 0.04	7*a*
3rd Segment				0.95	26.4	3.58	3.35†			0.88 ± 0.20	
500-600 Non-T	319	0.58	0.40	0.88	26.2	48.8	7.69	0.43 ± 0.02	0.40 ± 0.02	0.87 ± 0.12	7*b*

[a] : 1977-1992 dataset from *Okal and Romanowicz* [1994].
[b] : Updated 1977-2020 dataset.
[c] : 1977-1992 dataset from *Okal and Kirby* [1995].
[d] : Updated 1977-2020 dataset.

(1) There is essentially no difference, in terms of β-values, between "shallow" populations defined with a 75–km maximum depth (extending Okal and Romanowicz's (1994) study) or a 100-km one (extending Okal and Kirby's (1995)). For the latter case (Fig. 2*a*), the LSQ and MLE β-values fit perfectly the predicted $\beta = 2/3$ at lower moments, with a higher $\beta = 0.89$ (LSQ) past the critical moment $M_c = 10^{27.6}$ dyn*cm. The transition to Scholz' (1982) "*W*-model" of fault saturation in shallow seismogenic zones is confirmed by the high *F*-test value (63.9 as opposed to $F_{99} = 6.53$ for confidence at the 99% level). As such, our results reinforce, if need be, the notion that the fractal dimension *D* of shallow earthquakes is 2 ("earthquakes occur on faults"), and that their saturation for large moments follows Scholz' (1982) *W*-model.

(2) The 100–200 km bin features a strikingly similar two-segment distribution (Fig. 2*b*), with a smaller critical moment ($M_c = 10^{26.8}$ dyn*cm), reflecting a probable reduction in the average size of seismogenic zones at depth. The β-values computed from either the LSQ or MLE algorithms fit the values predicted for the *W*-model, and the high *F*-test value (84.6) confirms the bipartite nature of the distribution, being 12 times that required for confidence at the 99% level ($F_{99} = 7.21$). While Okal and Kirby (1995) had tentatively argued for a bipartite distribution, their smaller dataset (roughly 1/4 the population in the present study), and their analysis based on the simpler study of variance reduction, failed to robustly identify the similarity in behavior between the 0–100 km and 100–200 km bins, which can now be confidently asserted. Finally, we note that even though a simple visual reading of the distributions on Fig. 2*a* and 2*b* allows the identification of the elbow moment, the latter does correspond to a maximum in the *F*-test, as documented on Fig. 3 in the case of the 100–200 km depth bin. This property allows a more definitive resolution of the elbow in less obvious cases.

(3) In the 200–300 km bin, seismic activity decreases sharply, a classic trend continuing down to ~400 km (*e.g.*, Kirby et al., 1996b). As shown on Fig. 4*a*, the β-value remains essentially equal to 2/3 when regressed as a single segment. A slight change of behavior is observed around $10^{25.6}$ dyn*cm; even though the *F*-test suggests that it is significant ($F = 19.6$ *vs.* $F_{99} = 7.91$), it features a small reduction in the total number of events, and a greater irregularity in the distribution, rather than a significant change in slope. At the high-moment end of the population, the sharp drop observed in the last two bins is probably not significant, given that it implies a grand total of only 3 earthquakes, which we therefore exclude from the regressions. The slopes obtained using the MLE algorithm are also in general agreement with $\beta = 2/3$. Our results thus confirm those of Okal and Kirby (1995) ($\beta = 0.64$), who failed to document an elbow in population distribution for that depth bin, using a dataset about four times smaller. Its absence represents a change of behavior from the previous depth bin, but it could be affected by undersampling at and beyond a potential critical moment.

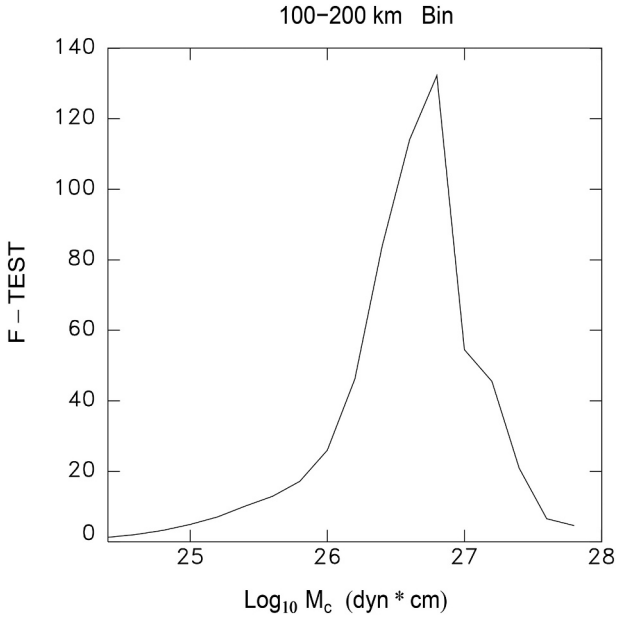

Fig. 3. Dependence of *F*-test on position of elbow moment M_c for a two-segment regression of the dataset on Fig. 2*b* (100–200 km). Note that the value resulting from a straight visual interpretation of the distribution on Fig. 2*b* also maximizes *F*.

(4) Results are very similar in the 300–400 km bin (Fig. 4*b*), with a total population of only 385 earthquakes (as opposed to just 110 in Okal and Kirby's (1995) study). Again, the regressed slopes are all close to 2/3 (Table 1), and a change of behavior to a more irregular distribution takes place around 10^{26} dyn*cm. However, a two-segment regression fails the *F*-test, even at the 90% level ($F = 0.55$ *vs.* $F_{99} = 8.18$ and $F_{90} = 2.83$). This case also illustrates the serious limitation of the MLE algorithm, which yields the unrealistic value $\beta = 0.11$ for the second (green) segment, totally controlled by the irregular populations of the first three bins of that segment. Our results are, again, unchanged with respect to Okal and Kirby's (1995) ($\beta = 0.63$).

When grouped together with the previous bin, a 200–400 km dataset features β-values all close to 2/3, with a possible break in the distribution around $10^{25.6}$ dyn*cm; while this feature passes the *F*-test (15.4 *vs.* $F_{99} = 7.91$), it again corresponds more to an offset in total population than to a change in the slope β. In this respect, the two bins (*3.*) and (*4.*) exhibit similar frequency-size relationships; they span a depth range where seismicity is generally at its lowest, and its origin least-well understood.

As such, our results underscore the artificial nature of the classic 300-km boundary between "intermediate" and "deep" earthquakes: the 200–300 and 300–400 km bins have more in common between themselves than with their neighbors immediately above or below. We have verified that splitting the 200–400 km depth range into 200–300 and 300–400 km bins fails an *F*-test ($F = 3.37$ *vs.* $F_{99} = 6.39$), while splitting a 100–300 km group at 200 km passes it ($F = 114$ *vs.* $F_{99} = 6.27$).

(5) The next depth bin (400–500 km; Fig. 5*a*) is the first to penetrate the transition zone below the first mantle discontinuity. It also features a low earthquake population (372 earthquakes), but the *F*-test now argues for a two-segment distribution ($F = 12.5$ *vs.* $F_{99} = 7.91$) with an elbow at $10^{25.8}$ dyn*cm. In this particular instance, the high-moment LSQ slope remains relatively high ($\beta = 0.81$), but the low-moment one becomes close to 1/2 (0.53), suggesting a significant change from the previous depth bins. The MLE slopes are generally very low (the high-moment one because of an irregular distribution of the smaller earthquakes controlling it), and once again, the MLE algorithm applied to a single segment fails to reveal the presence of an elbow. While a one-segment regression ($\beta = 0.64$) is close to Okal and Kirby's (1995) results ($\beta = 0.58$), these authors had not considered a two-segment model. When applied to their limited dataset of 120 earthquakes, that model indeed fails the *F*-test at the 99% confidence ($F = 6.24$ *vs.* $F_{99} = 9.42$), even though it yields slopes of $\beta = 0.50$ and 0.67 at low and high moments, respectively. These differences between our results and Okal and Kirby's (1995) probably reflect the irregular distribution of their limited

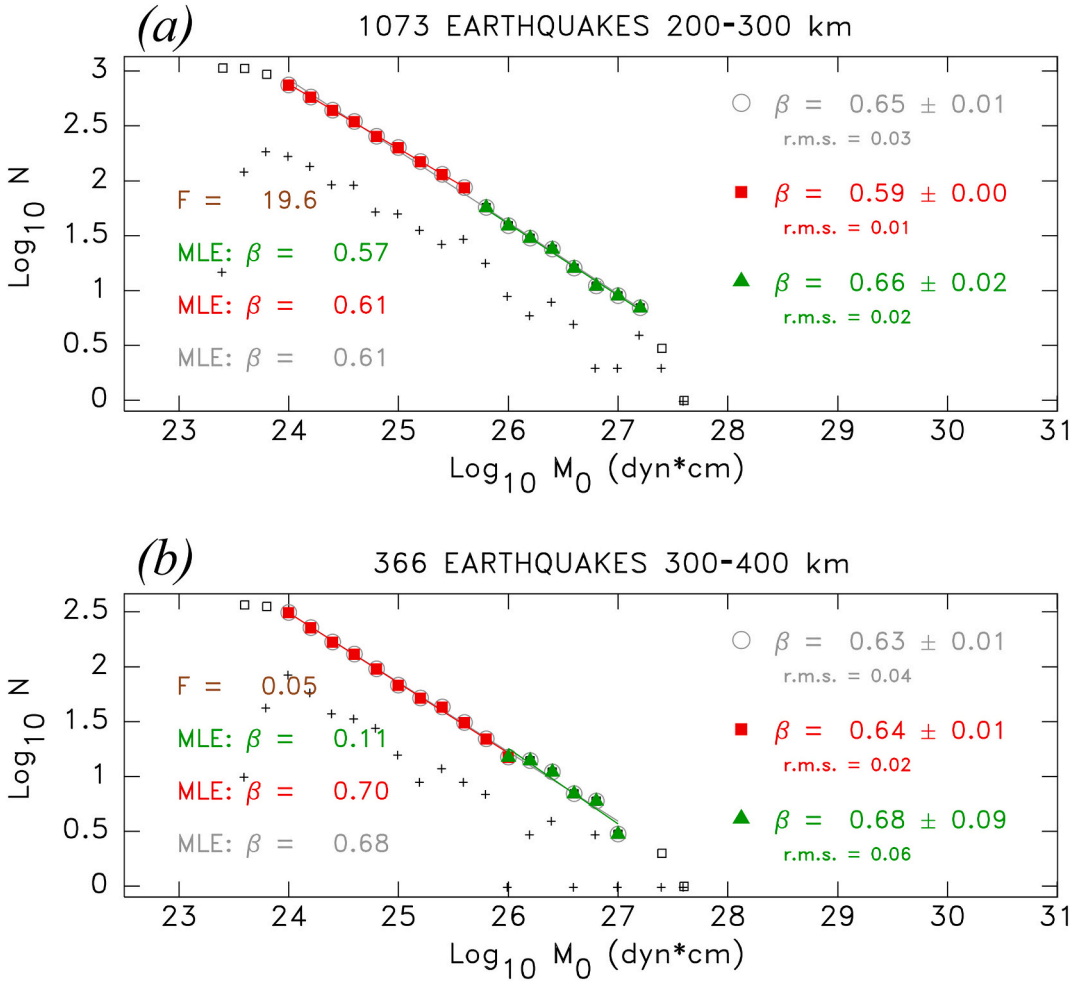

Fig. 4. Same as Fig. 2 for *(a)* the 200–300 km, and *(b)* the 300–400 km depth bins.

population in what constitutes our second segment.

In this context, and despite its relatively small size (372 events), we split the 400–500 km dataset into Tonga and non-Tonga earthquakes, following Okal and Kirby's (1995) approach at greater depths. We define "Tonga" as a box bounded by latitudes 40°S and 10°S and longitudes 175°E and 175°W. We recall that the motivation for earmarking that particular subduction zone is its exceptionally high thermal parameter (as much as $\Phi \approx 17{,}000$ km), nearby double that of its runner-up (Kirby et al., 1996b, Fig. 4). Furthermore, the abundant seismicity in Tonga allows meaningful frequency-size investigations which would become difficult in other, less active, subduction zones. A detailed discussion of the unique characteristics of the Tonga subduction zone is provided in Appendix B.

Fig. 5*b* and 5*c* show markedly different results for the Tonga and non-Tonga subsets. With a low-moment slope close to 2/3, the former generally follows the behavior of shallower depth bins, while the latter features a much reduced slope ($\beta = 0.50$). For both subsets there is a suggestion of saturation around $10^{26.2}$ dyn*cm, but this time, the presence of an elbow fails the most stringent *F*-test in Tonga ($F = 3.61$ *vs.* $F_{99} = 8.90$) and barely passes it ($F = 8.40$ *vs.* $F_{99} = 7.91$) outside Tonga.

(6) From 500 to 600 km, the dataset of 1026 earthquakes regresses in two segments with $\beta = 0.59$ and 0.99, respectively (Fig. 6*a*). The presence of an elbow at $M_c = 10^{26.2}$ dyn*cm is confirmed by the *F*-test ($F = 38.6$ *vs.* $F_{99} = 7.35$). MLE slopes for the low- and high-moment segments are 0.68 and 0.82, respectively, the difference between the LSQ and MLE slopes for the low-moment segment reflecting the slight curvature of the distribution. Our results are also somewhat different from those of Okal and Kirby (1995) ($\beta = 0.66$ at low moments and 1.94 at high ones, this last figure illustrating the absence, in their dataset, of any event above 10^{27} dyn*cm).

(7) The last depth bin ($h > 600$ km; Fig. 6*b*) features a striking difference with the results of Okal and Kirby (1995). The dataset used by these authors, which ended in 1992, comprised no earthquake greater than 9.6×10^{26} dyn*cm. Since then, no fewer than 14 events have occurred with $M_0 \geq 10^{27}$ dyn*cm, among them the famous 1994 Fiji, 1994 Bolivia, 1996 Flores, 2013 Okhotsk, 2015 Bonin and twin 2018 Tonga shocks. Our new dataset of 586 earthquakes (thrice Okal and Kirby's (1995)) features an elbow at 10^{27} dyn*cm (the upper bound of the previous dataset), significant at the 99% confidence level ($F = 9.48$ *vs.* $F_{99} = 6.98$) with slopes $\beta = 0.53$ and 0.71 at the low and high ends, respectively. The latter segment is poorly fit, with an irregular distribution of its bins. This is reflected in the MLE slopes, the low-end one being actually slightly steeper than at the high end.

4.2. *The case of the deep Tonga earthquakes*

Okal and Kirby (1995) observed different behaviors for Tonga and

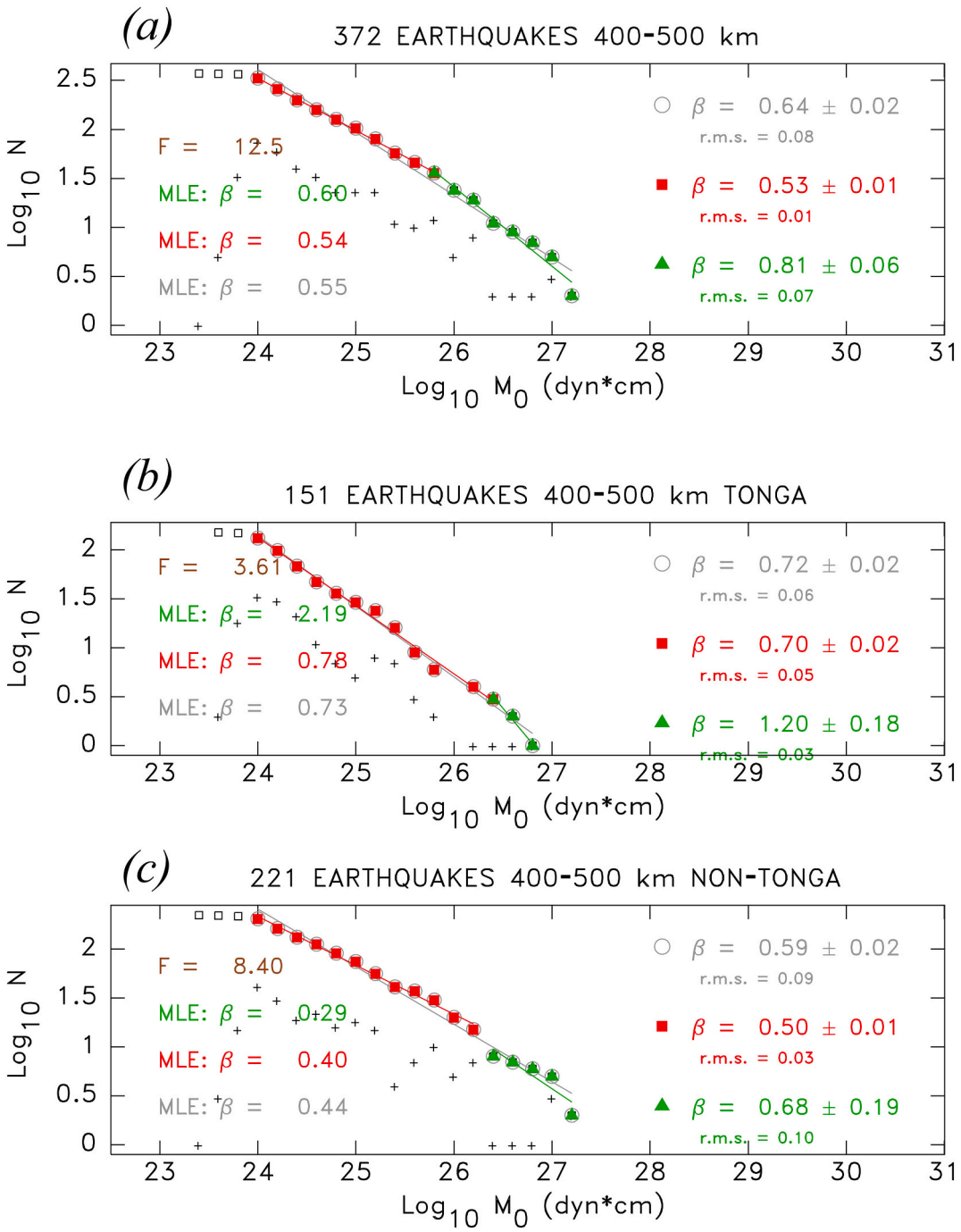

Fig. 5. *(a)*: Same as Fig. 2 for the 400–500 km bin; symbols as in Fig. 1. *(b)*: Same as (a) for the subset of Tonga earthquakes. *(c)*: Same as (a) for non-Tonga earthquakes. Note the different slopes at low moments in (b) and (c).

non-Tonga events in the 500–600 km bin, the former featuring a *decrease* in β-value for larger events, and the latter an *increase*. They went on to speculate that these observations could be reconciled by a three-step model of a three-dimensional seismogenic zone ($D = 3$), with a two-step earthquake saturation. Okal and Kirby's (1995) motivation stemmed mainly from the significantly colder regime of the Tonga slab (see above); in addition, that slab is unique as it sags extensively under the Fiji Plateau at depths of 500–600 km (Okal and Kirby, 1998). Under those conditions and as detailed in Appendix B, the seismogenic zone would be much larger in Tonga, which would displace the second elbow and the last, fully saturated regime towards higher moments unsampled by the reduced dataset available to their study. By contrast, in the warmer environment of non-Tonga WBZs, the first elbow would have taken place around 10^{24} dyn*cm, and the expected fully non-saturated regime below the threshold of completeness, where again, no regression is possible (Okal and Kirby, 1995, Fig. 7).

In this context, we again split our 500–600 km dataset into Tonga and non-Tonga subsets. In Tonga, Fig. 7*a* shows that the increase in the dataset available for large moments since Okal and Kirby's (1995) study makes it possible to resolve the second elbow in the distribution, with a slope $\beta = 0.95$ for the third segment, in excellent agreement with the proposed value $\beta = 1$. However, the slopes obtained at lower moments (0.83 and 0.73, respectively) are degraded with respect to Okal and Kirby (1995). The *F*-test value for the entire distribution ($F = 2.93$)

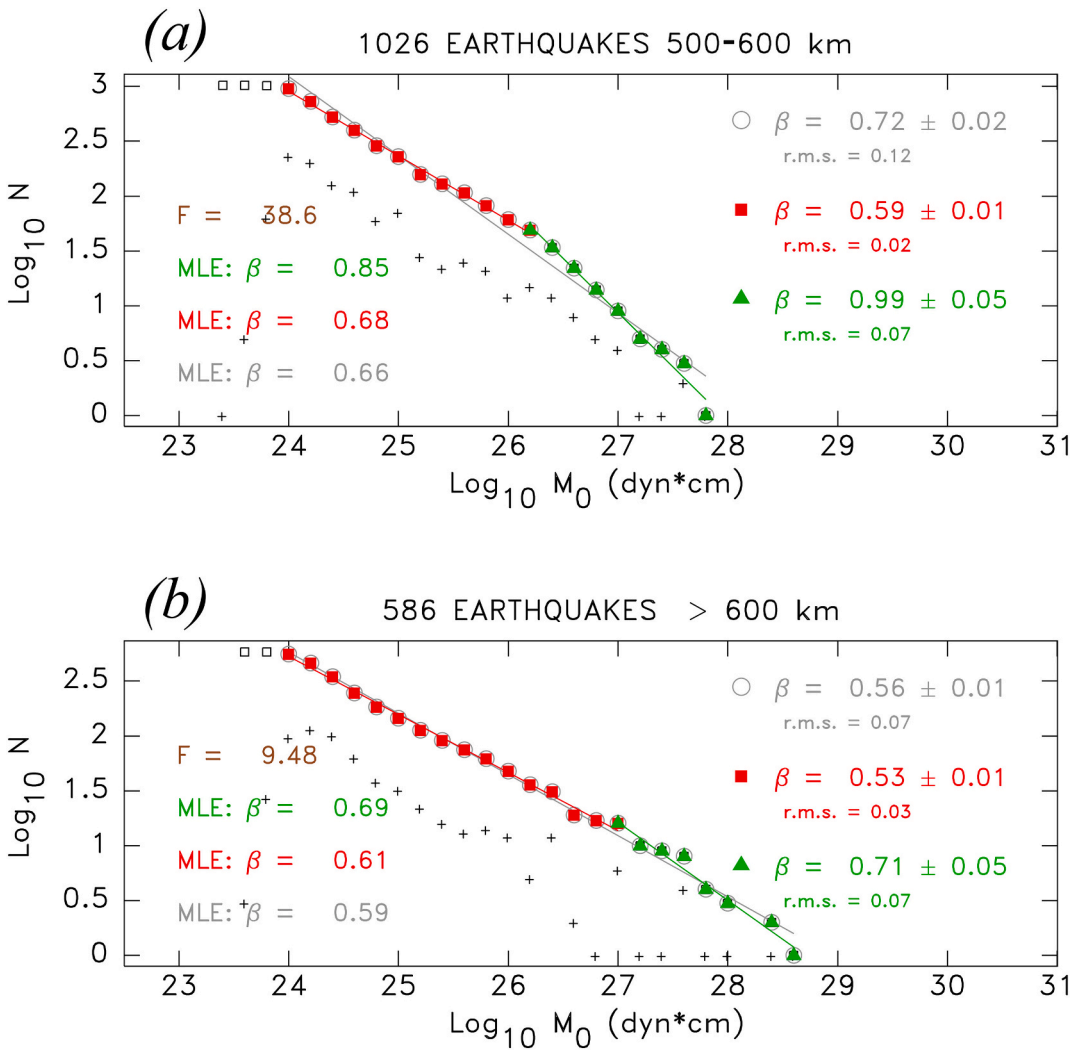

Fig. 6. Same as Fig. 2 for the 500–600 km *(a)*, and greater than 600 km *(b)* depth bins.

corresponds to a confidence level of 93.8%; for the second and third segment, $F = 3.58$, meaning a confidence level of 91.0% for the presence of the second elbow at $10^{26.5}$ dyn*cm. Finally, in the presence of irregularities in the distribution, the MLE values are poor descriptors of the slopes of the various segments.

By contrast, the distribution of non-Tonga events in the 500–600 km bin (Fig. 7*b*) remains essentially equivalent to Okal and Kirby's (1995), the slope of the second segment ($\beta = 0.88$) falling slightly below the theoretical value of 1, as opposed to slightly above it in their study (1.17), such fluctuations being largely controlled by the occurrence of just two very large events. The *F*-test confirms the presence of an elbow around 10^{26} dyn*cm ($F = 48.8$ *vs.* $F_{99} = 7.69$). Once again, the MLE values appear scattered in the presence of irregular distributions.

The bottom line of this experiment is that the substantial increase (187%) in the size of the dataset since Okal and Kirby's (1995) study supports the model proposed by these authors, namely the presence of the second elbow in Tonga, which they could not resolve because of undersampling at the relevant large moments. The distribution of non-Tonga events, also increased by 182%, remains identical because its proposed first segment at lower moments is unresolvable due to incompleteness, a situation unchanged by a mere increase in population.

4.3. The possible effect of focal geometry on frequency-size relationships

We recall that close to 30 years ago, Frohlich and Davis (1993) suggested that shallow normal-faulting (NO) earthquakes feature *b*-values higher by about 0.2 units than their thrust (TH) or strike-slip (SS) counterparts. This was confirmed by Okal and Romanowicz (1994), with β-values (before saturation) of 0.73, 0.64 and 0.71, respectively, for NO, TH and SS mechanisms (we note that these studies both defined NO and SS mechanisms as featuring **P** and **N** axes dipping 60° or more, while TH events required a **T** axis dipping only 50°). More recently, Schorlemmer et al. (2005) similarly investigated a number of shallow global and regional datasets, and concluded that NO events featured *b*-values higher than TH ones by up to 0.4 unit; we note, however, that in their study the GlobalCMT dataset ("Harvard" at the time) featured a difference of only ~ 0.25 unit (equivalent to 0.17 unit of β). Such results were later interpreted by Scholz (2015) in the context of a more general anti-correlation of *b*-values with differential stress.

As summarized on Fig. 8, we generally uphold these results with slopes β of 0.71 and 0.63 for NO and TH, but as much as 0.75 for SS from updated, much larger shallow CMT datasets. We note, however that the distributions of the larger events become more irregular in each of the individual geometries.

When exploring the possible extension of these results to intermediate and deep earthquakes, we rotate the orientation of each focal mechanism with respect to the local direction of steepest descent of the slab in the Slab2 dataset (Hayes et al., 2018). We then qualify the earthquake as Down-dip Compressional (DC), Tensional (DT), or Neutral (DN) when its **P**, **T**, or **N** axis, respectively, makes an angle of less than

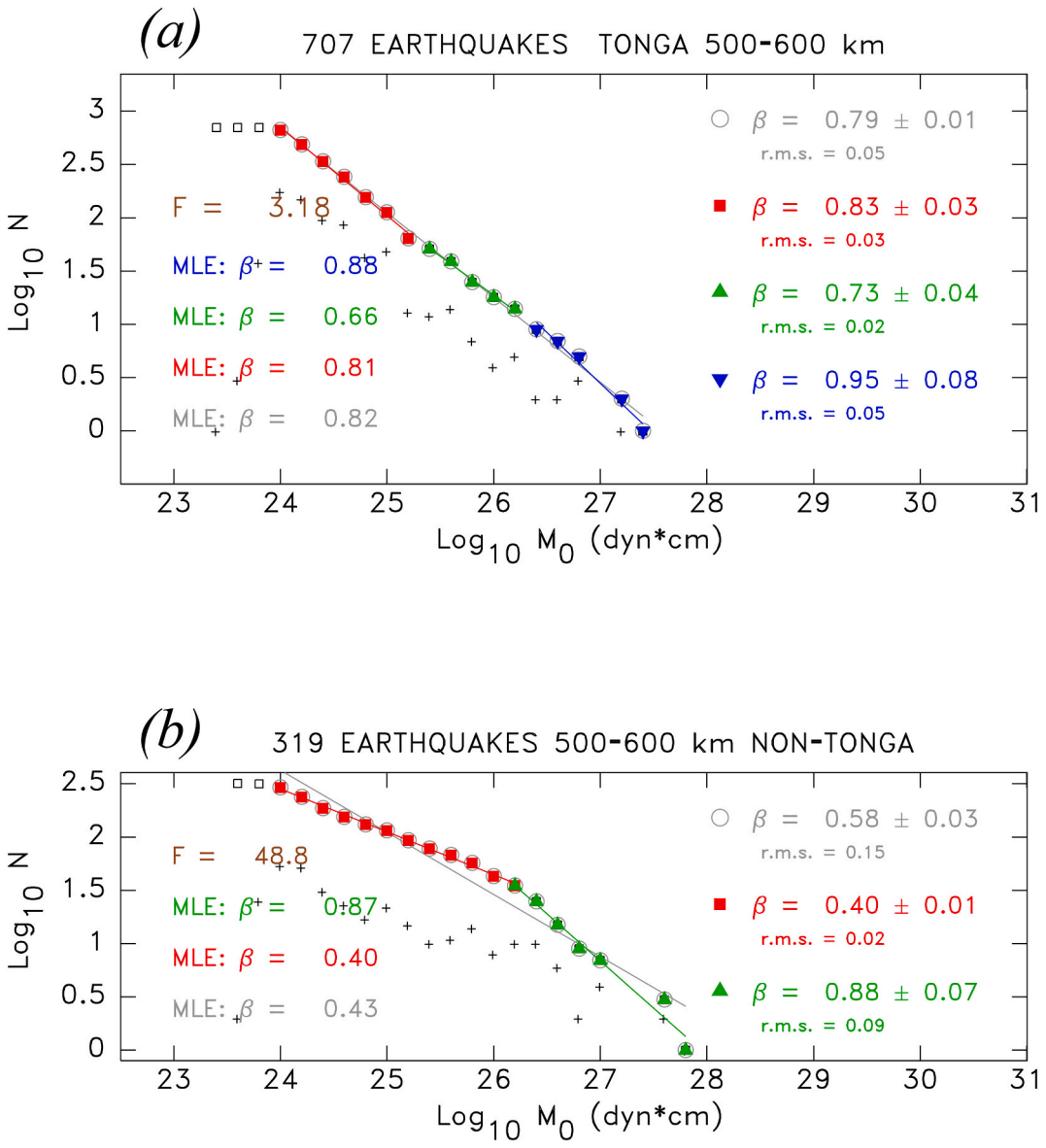

Fig. 7. Same as Fig. 5*a* for Tonga *(a)* and Non-Tonga *(b)* subsets of the 500–600 km bin.

($\cos^{-1}\sqrt{2/3} = 35.3°$) with the slab's down-dip vector. Earthquakes failing all three categories are categorized as Hybrid (HY). In addition to relating them directly to the local geometry of the subduction, and as discussed in Saloor and Okal (2018), this classification provides a more balanced distribution of focal mechanisms, with a random geometry of the focal sphere standing an equal chance (18%) of being DC, DT or DN (and 45% HY). Our approach also eliminates the need to examine both fault planes of a given mechanism, as certain hybrid geometries could for example qualify as TH along one fault-plane, and SS along the other, when based on rake angles. We then process the resulting datasets with our standard frequency-moment algorithm, with results listed in Table 2.

We first note that the number of earthquakes in the various categories varies strongly inside each depth bin. In several instances, we find populations dominated by a particular geometry. For example, mechanisms are primarily Down-dip Tensional (DT) in the 100–200 km and 200–300 km bins (both 43% of solutions) and overwhelmingly Down-dip Compressional (DC) in the 500–600 km (68%) and < 600 km (69%) bins. This classic property is widely interpreted as expressing the release of slab pull in the shallow portion of the slab and the resistance to penetration of the deep mantle in its lower parts, a general framework first proposed by Isacks and Molnar (1971). Hybrid (HY) groups consistently feature high populations, with a large proportion trending towards the majority group (DT or DC) and being classified as HY only out of the necessity to impose a threshold on the angle between the relevant stress axis and the down-dip direction. Under such conditions, several depth-mechanism combinations hold populations of only a few tens of mostly small earthquakes, clearly insufficient to perform a frequency-moment analysis. They are labeled as "insufficient" in Table 2.

- As shown on Fig. 9 and detailed in Table 2, results are more confused in the 100–200 km depth bin. For the 2036 DT events, the slope beyond the elbow at $10^{26.6}$ dyn*cm ($\beta = 0.79 \pm 0.08$) is significantly lower than for the whole dataset ($\beta = 0.94 \pm 0.04$; Fig. 2*b*). The presence of the elbow fails the most stringent *F*-test ($F = 5.08$ *vs.* $F_{99} = 7.51$) and the large-moment population is particularly irregular and controlled by two relatively large events, including the largest known intermediate-depth CMT solution (Peru, 26 May 2019). The 669 DC earthquakes have comparable features (except for the larger events), and again fail the *F*-test for the presence of an elbow in the

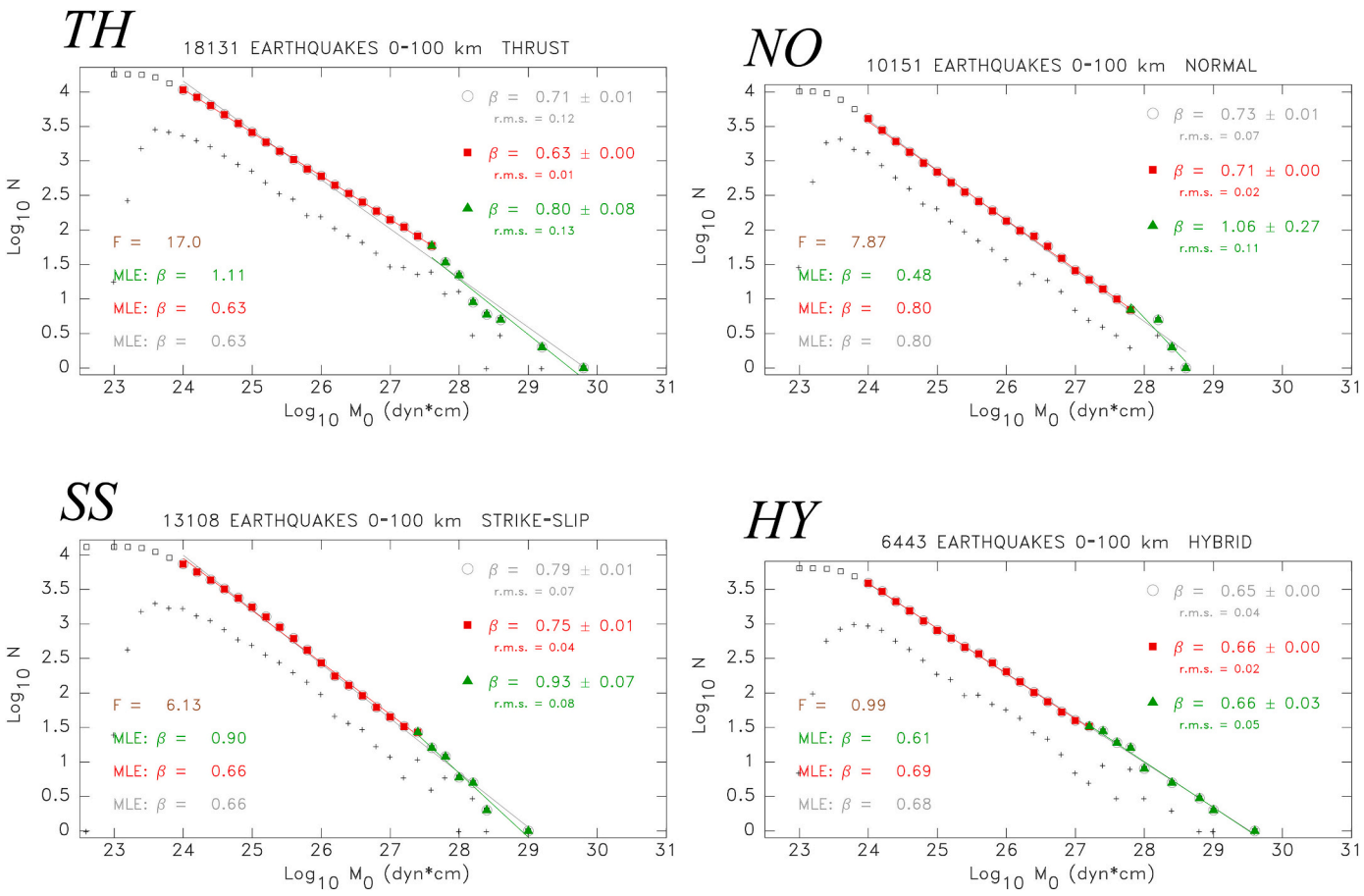

Fig. 8. Population distributions of the 0–100 km depth bin (Fig. 2*a*), separated by focal mechanism: *TH*: Thrust; *NO*: Normal; *SS*: Strike-slip; *HY*: Hybrid. Symbols as in Fig. 2.

Table 2
Datasets sorted by focal mechanism.

Depth bin (km) and Mechanism	Number of events	β (LSQ)						β (MLE)			Figure
		All	$M_0 < M_c$	$M_0 > M_c$	$\log_{10} M_c$(dyn*cm)	F Test	F_{99}(†: F_{90})	All	$M_0 < M_c$	$M_0 > M_c$	
0-100 TH	18131	0.71	0.63	0.80	27.6	17.0	6.72	0.63 ± 0.01	0.63 ± 0.01	1.11 ± 0.15	8
0-100 NO	10151	0.73	0.71	1.06	27.8	7.87	6.98	0.80 ± 0.01	0.80 ± 0.01	0.72 ± 0.13	8
0-100 SS	13108	0.79	0.75	0.93	27.4	6.13	2.63†	0.67 ± 0.01	0.66 ± 0.01	0.97 ± 0.16	8
0-100 HY	6443	0.65	0.66	0.66	27.2	0.99	2.62†	0.68 ± 0.01	0.69 ± 0.01	0.61 ± 0.08	8
100-200 DT	2036	0.71	0.66	0.79	26.8	5.08	2.73†	0.67 ± 0.02	0.69 ± 0.02	1.09 ± 0.22	9
100-200 DC	669	0.66	0.63	0.89	26.8	2.84	2.76†	0.65 ± 0.03	0.65 ± 0.03	0.79 ± 0.17	9
100-200 DN	391	0.72	0.75	0.65	26.6	0.81	2.88†	0.82 ± 0.06	0.81 ± 0.04	0.57 ± 0.12	9
100-200 HY	1566	0.68	0.62	0.87	26.8	11.3	7.51	0.64 ± 0.02	0.65 ± 0.02	0.77 ± 0.14	9
200-300 DT	462	0.60	0.54	0.64	25.6	9.81	8.18	0.57 ± 0.03	0.58 ± 0.02	0.70 ± 0.08	
200-300 DC	221	0.79	0.62	1.11	25.6	12.1	9.42	0.67 ± 0.05	0.69 ± 0.04	1.24 ± 0.35	
200-300 DN	75	Insufficient									
200-300 HY	299	0.68	0.65	0.69	25.6	0.30	2.88†	0.65 ± 0.04	0.66 ± 0.03	0.08 ± 0.01	
300-400 DC	154	0.60	0.65	0.71	25.8	1.51	2.88†	0.58 ± 0.05	0.67 ± 0.05	0.13 ± 0.01	
300-400 DT	47	Insufficient									
300-400 DN	26	Insufficient									
300-400 HY	134	0.62	0.73	0.29	25.6	25.9	24.5	0.80 ± 0.07	0.83 ± 0.06	0.70 ± 0.26	
400-500 DC	209	0.63	0.54	0.80	25.8	6.31	2.79†	0.55 ± 0.04	0.58 ± 0.03	0.28 ± 0.02	
400-500 DT	20	Insufficient									
400-500 DN	22	Insufficient									
400-500 HY	97	0.54	0.50	0.64	26.0	10.5	8.90	0.51 ± 0.05	0.51 ± 0.03	1.39 ± 0.58	
500-600 DC	693	0.65	0.56	0.75	26.2	17.3	7.21	0.63 ± 0.03	0.67 ± 0.02	0.71 ± 0.10	
500-600 DT	19	Insufficient									
500-600 DN	38	Insufficient									
500-600 HY	264	0.66	0.67	0.75	26.2	0.18	2.93†	0.76 ± 0.05	0.78 ± 0.53	1.35 ± 0.27	
>600 DC	402	0.53	0.49	0.57	26.4	3.10	2.69†	0.56 ± 0.03	0.59 ± 0.03	0.61 ± 0.11	
>600 DT	7	Insufficient									
>600 DN	17	Insufficient									
>600 HY	131	0.70	0.88	0.55	25.4	11.0	3.20†	0.80 ± 0.07	0.72 ± 0.04	0.56 ± 0.15	

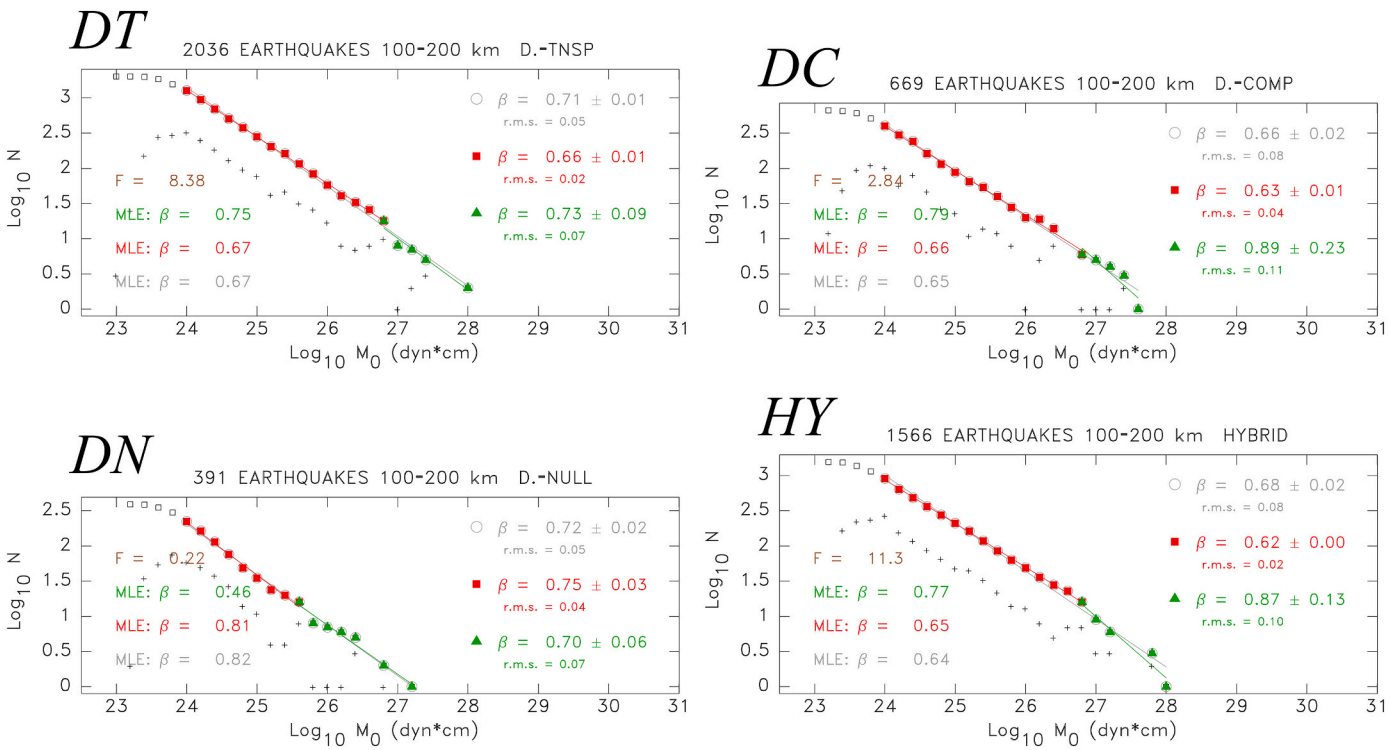

Fig. 9. Population distributions of the 100–200 km depth bin (Fig. 2*b*), separated by focal mechanism: *DT*: Down-dip tensional; *DC*: Down-dip compressional; *DN*: Down-dip neutral; *HY*: Hybrid. Symbols as in Fig. 2.

distribution, with a one-segment $\beta = 0.66 \pm 0.02$ indistinguishable from a theoretical 2/3. The more populated HY dataset features results very similar to DT ($\beta = 0.62 \pm 0.01$ and 0.87 ± 0.13), with a passing *F*-test at the 99.35% level. Only the DN dataset suggests slightly higher values ($\beta = 0.70 \pm 0.06$), but it features an irregular distribution, and fails the *F*-test for an elbow, even at the 50% level. The conclusion of our experiment for that depth bin is that there is no clear evidence of a dependence of frequency-moment statistics on focal mechanism.

- In the well-populated 500–600 km depth bin, the DC group is so dominant (68%) that its frequency-size properties are expectedly very similar to those of the global population ($\beta = 0.56 \pm 0.01$ and 0.73 ± 0.03); the HY group has an irregular distribution failing an *F*-test for the presence of an elbow, and the other groups (DT and DN) are insufficiently populated for analysis (respectively 19 and 35 events). Similar conclusions are obtained for events deeper than 600 km, and tentatively in the intermediate depth bins where the populations are often too low to reach meaningful conclusions for several focal geometries.

The conclusion of this section is that we fail to document a systematic effect of focal mechanism on frequency-moment statistics for intermediate and deep earthquakes, but the analysis could be somewhat biased by the fact that those events have a non-random orientation of their mechanisms. Nevertheless and in this context, our results would suggest that the dependence observed for shallow earthquakes (Frohlich and Davis, 1993; Okal and Romanowicz, 1994; Schorlemmer et al., 2005) may express a difference between interplate and intraplate environments, notably in the context of Scholz' (2015) model, rather than the strict effect of focal geometry; a similar conclusion was reached regarding energy-to-moment ratios by Saloor and Okal (2018).

4.4. Are "short" slabs different?

In this section, we look for any possible difference in populations in the shallower depth bins between those slabs whose seismicity terminates above 300 km (*e.g.*, Ryukyu, Aleutian, Central America), and those which fully extend to greater depths (*e.g.*, Tonga, Kuriles, South America). We are motivated by the fact that the presence of a fully developed slab could modify the slab pull stresses in its upper part, and possibly affect the frequency-size relations, in the framework of Scholz' (2015) model.

Results are listed in Table 3 and shown on Fig. 10. In the 100–200 km depth band, the new slopes are all within 0.02 units of those for the full depth bin (see Table 1). In the 200–300 km depth bin, a weak trend may be present in the two-segment regressions past the elbows, with short slabs showing slightly weaker values of β, albeit with a very irregular distribution failing the *F*-test even at the 90% confidence level ($F = 1.80$ *vs.* $F_{90} = 2.88$), and the long slabs slightly higher ones. In summary, short and long slabs do not exhibit markedly different frequency-moment properties (See Table 3).

5. Results for oceanic intraplate provinces interpreted as ancestors to slabs

In this section, we examine frequency-size relations for several oceanic intraplate regions, which can be regarded as ancestors to slabs before the oceanic lithosphere reaches a subduction zone. We seek to determine if the populations of earthquakes generated inside the same material, before and immediately after it subducts (*e.g.*, for $h \leq 200$ km), behave similarly. We are motivated by recent studies which argued that intermediate-depth seismicity could be correlated to hydration during bending as the plate approaches the trench (Ranero et al., 2003; Okazaki and Hirth, 2016; Boneh et al., 2019).

In a previous study, Okal and Sweet (2007) investigated frequency-size relations for intraplate earthquakes and concluded that their β-values were similar to those of interplate events ($\beta \approx 2/3$; their Fig. 2C). However, their study targeted "true" intraplate earthquakes located at least 400 km from a plate boundary, in both oceans and continents. They excluded zones of intense deformation (such as the

Table 3
Possible influence of slab extent.

Depth bin (km) and Slab Extent	Number of events	β (LSQ)						β (MLE)			Figure
		All	$M_0 < M_c$	$M_0 > M_c$	$\log_{10} M_c$ (dyn*cm)	F Test	F_{99} (†: F_{90})	All	$M_0 < M_c$	$M_0 > M_c$	
100-200 SHORT	1397	0.72	0.67	0.93	26.8	8.28	7.51	0.66 ± 0.02	0.66 ± 0.02	1.44 ± 0.41	10
100-200 LONG	3330	0.72	0.65	0.92	26.8	39.0	7.21	0.68 ± 0.02	0.68 ± 0.01	0.71 ± 0.09	10
200-300 SHORT	235	0.65	0.59	0.57	25.8	1.80	2.88†	0.55 ± 0.03	0.45 ± 0.02	0.71 ± 0.09	10
200-300 LONG	838	0.66	0.61	0.74	25.8	9.73	7.91	0.63 ± 0.03	0.63 ± 0.02	0.50 ± 0.04	10

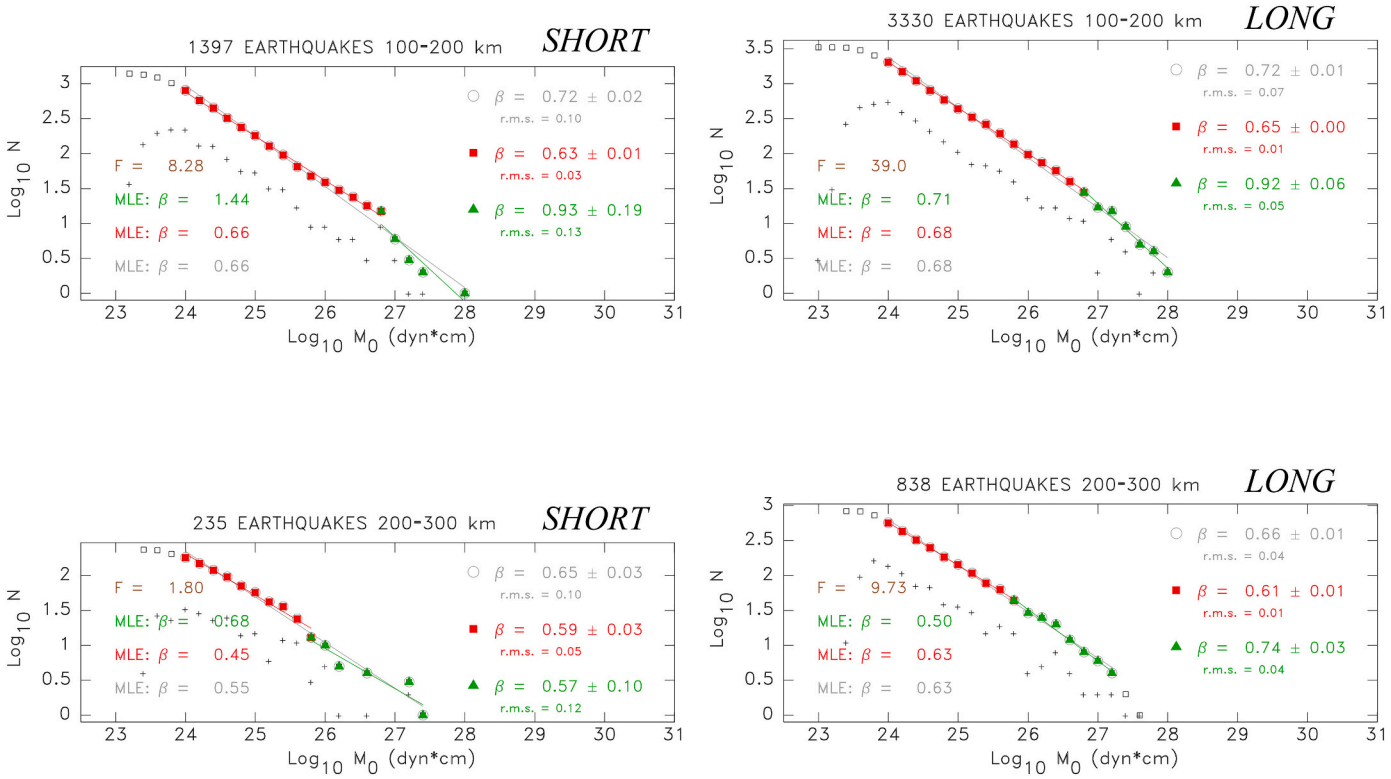

Fig. 10. Population distributions of the 100–200 km *(Top)* and 200,300 km *(Bottom)* bins, separated into *short* slabs with seismicity not extending beyond 300 km *(Left)*, and longer ones *(Right)*. See text for details. Symbols as on Fig. 2.

Basin and Range Province or most of China), as well as diffuse plate boundaries (such as India-Australia) and events associated with hotspot volcanism (*e.g.*, in Hawaii). This resulted in a dataset of only 218 earthquakes with a maximum moment of 4×10^{26} dyn*cm, which is less than the elbow moment of the global shallow population (Fig. 2*a*). Also, their study deliberately excluded regions affected by nearby plate boundaries, where ancillary phenomena such as bending in the outer rises can take place.

5.1. *Outer rise earthquakes in the vicinity of subduction zones*

By contrast, we first target here intraplate earthquakes located at the margins of subduction zones, which were excluded by Okal and Sweet (2007). Our database was built by defining subduction zone segments, interpolated to a sampling of 10 km from Bird's (2003) catalog of plate boundaries, and retaining all GlobalCMT shallow events ($h < 100$ km) located on the outer side of the boundary, at most 300 km but not closer than 30 km from a segment. This resulted in a dataset of 1453 earthquakes with a maximum moment of 1.8×10^{28} dyn*cm (13 January 2007; normal faulting Kuril earthquake); we eliminated from the dataset the region off Sumatra (including the large 2012 events), which may not be genuinely intraplate, as it nears the diffuse India-Australia boundary. We refer to the resulting dataset as "outer rise" earthquakes, even though such features can be absent from the morphology of poorly coupled subduction systems, such as the Mariana Trench (Uyeda and Kanamori, 1979), where the plate nonetheless undergoes bending.

As shown on Fig. 11*a* and Table 4, the population of outer rise earthquakes features β-values significantly different from both the full shallow GlobalCMT dataset (Fig. 2*a*) and the first bin of intermediate depth earthquakes (Fig. 2*b*). Namely, at small moments, $\beta = 0.62$ is intermediate between the slopes 2/3 and 1/2 that are predictable from various combinations of integer values of D and $1/\lambda$ (Section 1). An elbow is present around 10^{26} dyn*cm, beyond which β *decreases* to values closer to 1/2, the change in behavior being confirmed by the F-test ($F = 7.83$ *vs.* $F_{99} = 7.21$).

The outer rise population is dominated by normal faulting events (making 61% of the total), which express the release of tensional stresses associated with the bending of the upper part of the plate as it enters the subduction zone (Stauder, 1968; Chapple and Forsyth, 1979). Not surprisingly, given their preponderance (about 2/3 of the dataset), these events feature the same behavior as the global outer rise population (Fig. 8*b*). A meager dataset of 184 outer rise thrust events, generally interpreted as expressing the compression of the deeper part of the lithosphere under bending, also shows a reduction of β from close to 2/3 at lower moments to a value approaching 1/2 beyond a surprising gap of earthquakes around 10^{26} dyn*cm, which probably reflects

undersampling in an insufficient dataset (Fig. 11*c*).

Our results would then suggest that outer rise earthquakes undergo saturation following Scholz' (1982) *L*-model, in which the slip Δu continues to grow after fault width has saturated ($D = 1$; $\lambda = 1/2$).

5.2. Mid-plate oceanic earthquakes

Moving backwards in the history of oceanic plates, we consider next "truly" intraplate earthquakes by updating Okal and Sweet's (2007) study, but restricting it to oceanic earthquakes. These authors' dataset contained only 218 intraplate events, including earthquakes in stable continental areas. Here, we consider all oceanic GlobalCMT earthquakes (1977-September 2020) satisfying these authors' intraplate criterion, *i.e.*, being at least 400 km from the nearest plate boundary. This results in a dataset of 322 earthquakes with, remarkably, only one event larger than in Okal and Sweet's (2007) study, the 2015 Antarctica plate earthquake near the Kerguelen Islands.

Our results ($\beta = 0.66$; Fig. 12) are comparable to those of Okal and Sweet (2007), the distribution being also similarly irregular. The only difference would stem from the 2015 Antarctica plate earthquake, which could suggest saturation under Scholz' (1982) *W*-model, but its lone character makes any interpretation speculative.

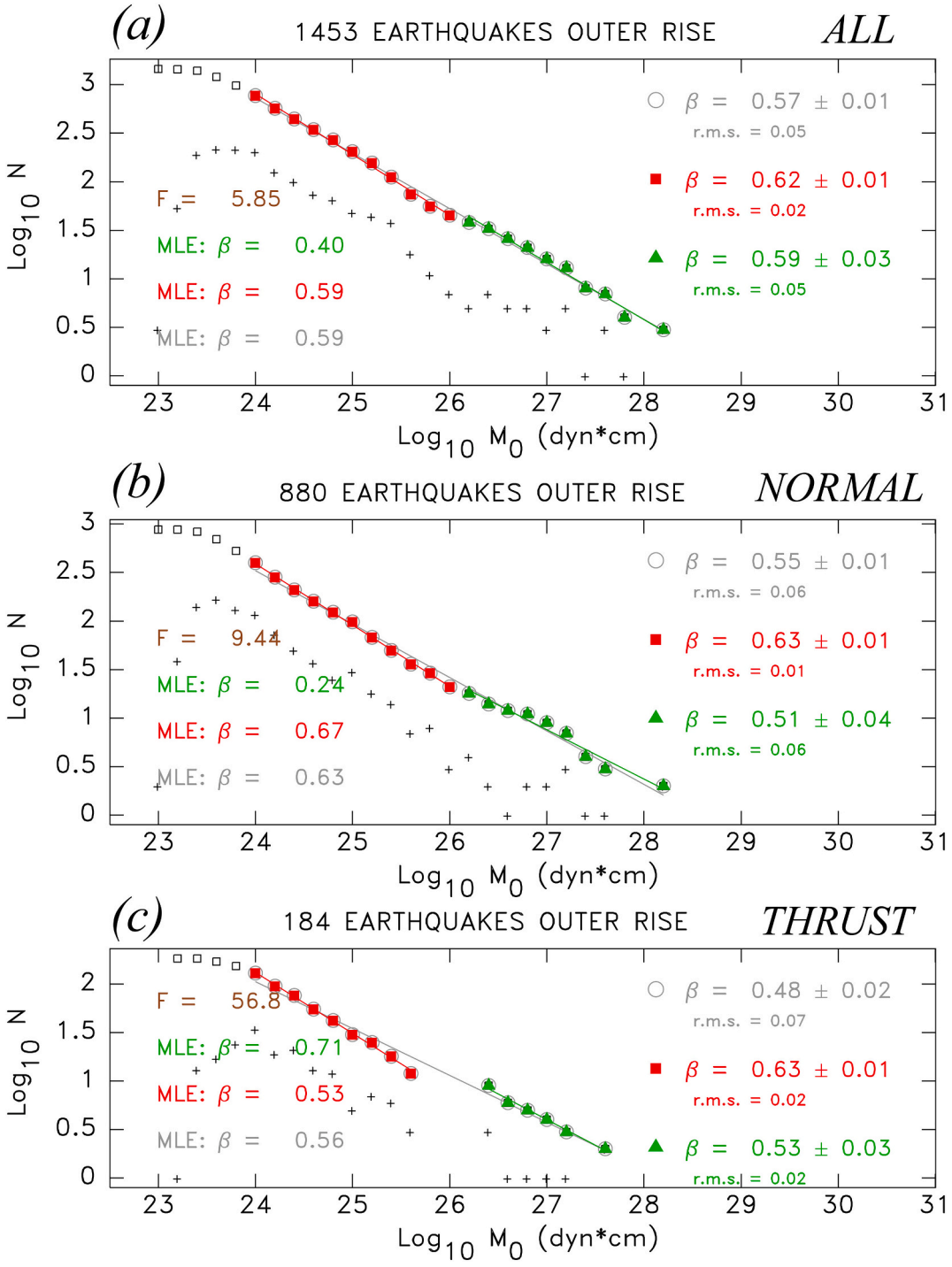

Fig. 11. Populations of outer rise earthquakes occurring intraplate between 30 and 300 km seaward of a subduction zone. *(a)*: All mechanisms; *(b)*: Normal faulting events; *(c)*: Thrust faulting events. Symbols as in Fig. 2.

Table 4
Results for additional datasets outside subduction zones.

Region	Number of events	β (LSQ)						β (MLE)			Figure
		All	$M_0 < M_c$	$M_0 > M_c$	$\log_{10} M_c$ (dyn*cm)	F Test	F_{99} (†: F_{90})	All	$M_0 < M_c$	$M_0 > M_c$	
Outer-Rise All	1453	0.55	0.62	0.59	26.0	7.83	7.21	0.59 ± 0.02	0.59 ± 0.02	0.40 ± 0.04	11*a*
Outer-R. Normal	880	0.55	0.63	0.51	26.0	9.44	7.35	0.63 ± 0.03	0.67 ± 0.03	0.24 ± 0.02	11*b*
Outer-R. Thrust	184	0.48	0.63	0.53	Gap	56.8	8.50	0.57 ± 0.05	0.53 ± 0.03	0.54 ± 0.11	11*c*
True Intraplate	322	0.67	0.66	1.76	26.4	6.47	2.93	0.68 0.05	0.70 0.05	1.63 0.04	12
Near MOR (30-300)	653	1.19	1.07	3.95	25.6	22.1	3.20	1.04 ± 0.06	0.70 ± 0.05	1.80 ± 0.51	13*a*
Near MOR (20-300)	1131	1.31	1.22	1.95	25.6	12.2	3.20	1.17 ± 0.05	1.16 ± 0.05	1.80 ± 0.51	13*b*
Near MOR (20-30)	478	1.85	1.70	2.38	25.0	1.49	4.48	1.47 ± 0.10	1.31 ± 0.08	Insufficient	13*c*
True MOR	2490	1.42	1.64	0.75	25.4	4.19	3.57	1.37 ± 0.05	1.32 ± 0.04	1.34 ± 0.83	13*d*

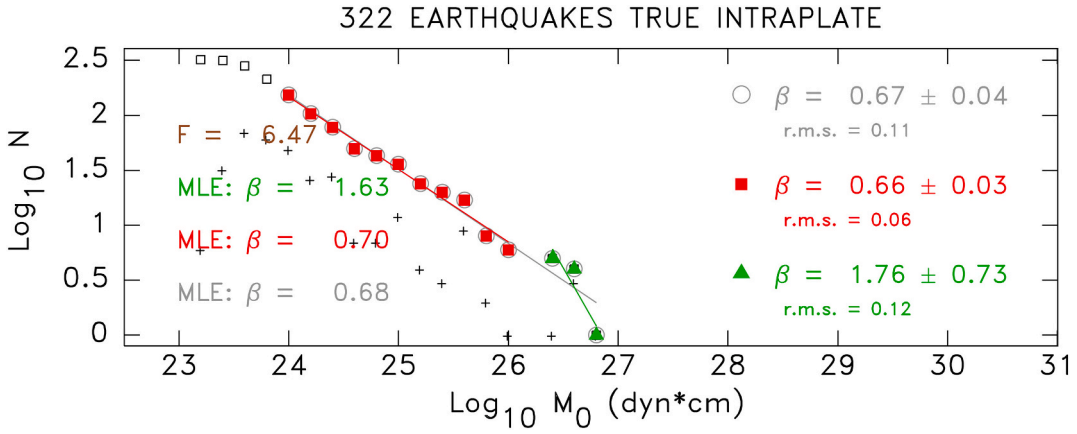

Fig. 12. Populations of true intraplate oceanic earthquakes, occurring at least 400 km from the nearest plate boundary. Symbols as in Fig. 2.

5.3. *Intraplate seismicity in the vicinity of Mid-Oceanic Ridges*

Finally, we examine intraplate seismicity in the youngest part of oceanic lithosphere, namely in the vicinity of Mid-Oceanic Ridges, initially at a distance of 30 to 300 km from the nearest plate boundary. We focus on normal-faulting events, which constitute the bulk of such seismicity (Wiens and Stein, 1984; Bergman and Solomon, 1984). The lower bound is chosen to guard against including earthquakes directly associated with the spreading process. As shown on Fig. 13*a*, the resulting LSQ and MLE β-values (1.07 and 0.99, respectively, excluding the largest two events) would argue for a physical value of 1, interpretable under Rundle's (1989) model (see Section 1).

If the domain of study is extended 10 km towards the ridges, the population is significantly increased (by 73%), and the LSQ value is now larger ($\beta = 1.22$; Fig. 13*b*). This is confirmed by processing the difference between the two datasets, namely those events located between 20 and 30 km of the plate boundary: their population distribution features significant curvature and β-values trending towards 2 for the largest events (Fig. 13*c*).

This change in β-value between the datasets in Fig. 13*a* and 13*b* simply expresses that plate boundary processes at mid-ocean ridges take place over a finite width, exemplified at the slow-spreading ridges by the axial valley (Luyendyk and Macdonald, 1977). Indeed, in Fig. 13*d*, we extend the study to truly interplate mid-oceanic ridge earthquakes, defined as occurring within 20 km of the plate boundary as defined by Bird (2003), and find similar β-values, between 1.5 and 2. The commonality between Figs. 13*c* and 10*d* expresses that earthquakes directly associated with spreading extend about 30 km away from the boundary.

6. Discussion and conclusion: the seismic times and lives of oceanic lithosphere

We discuss our results in the framework of the evolution of oceanic lithosphere, from its generation at the mid-oceanic ridges, through its transit across oceanic basins, until its subduction and eventual penetration through the transition zone.

6.1. *At the ridge or in its immediate vicinity*

Within 30 km of the plate boundary, we observe β values ranging from 1.5 to 2 (Fig. 13*c, d*). We have verified the presence of some degree of regional heterogeneity in the distribution, with the highest values ($\beta = 2$) occurring in the vicinity of the faster spreading ridges; however, the fastest segments are known to spread aseismically, at the threshold of worldwide detection ($m_b \geq 4.5$) or of the GlobalCMT catalog (10^{24} dyn*cm) and probably at even lower magnitudes (Tréhu and Solomon, 1983), with detectable events concentrated in anomalous areas such as overlapping spreading centers (Wilcock et al., 1992). Under those conditions, it is difficult to formally quantify the matter further.

High values of β could be explained by either a 3-dimensional seismic zone saturating under Scholz' (1982) L-model ($D = 3$; $\lambda = 1/2$) or a system of small faults saturated under the W-model ($D = 2$; $\lambda = 1$).

6.2. *In the proximity of the ridge*

Between 30 and 300 km from the ridge, the value $\beta \approx 1$ (Fig. 13*a*) can be interpreted as unsaturated earthquakes occurring in a 3-dimensional

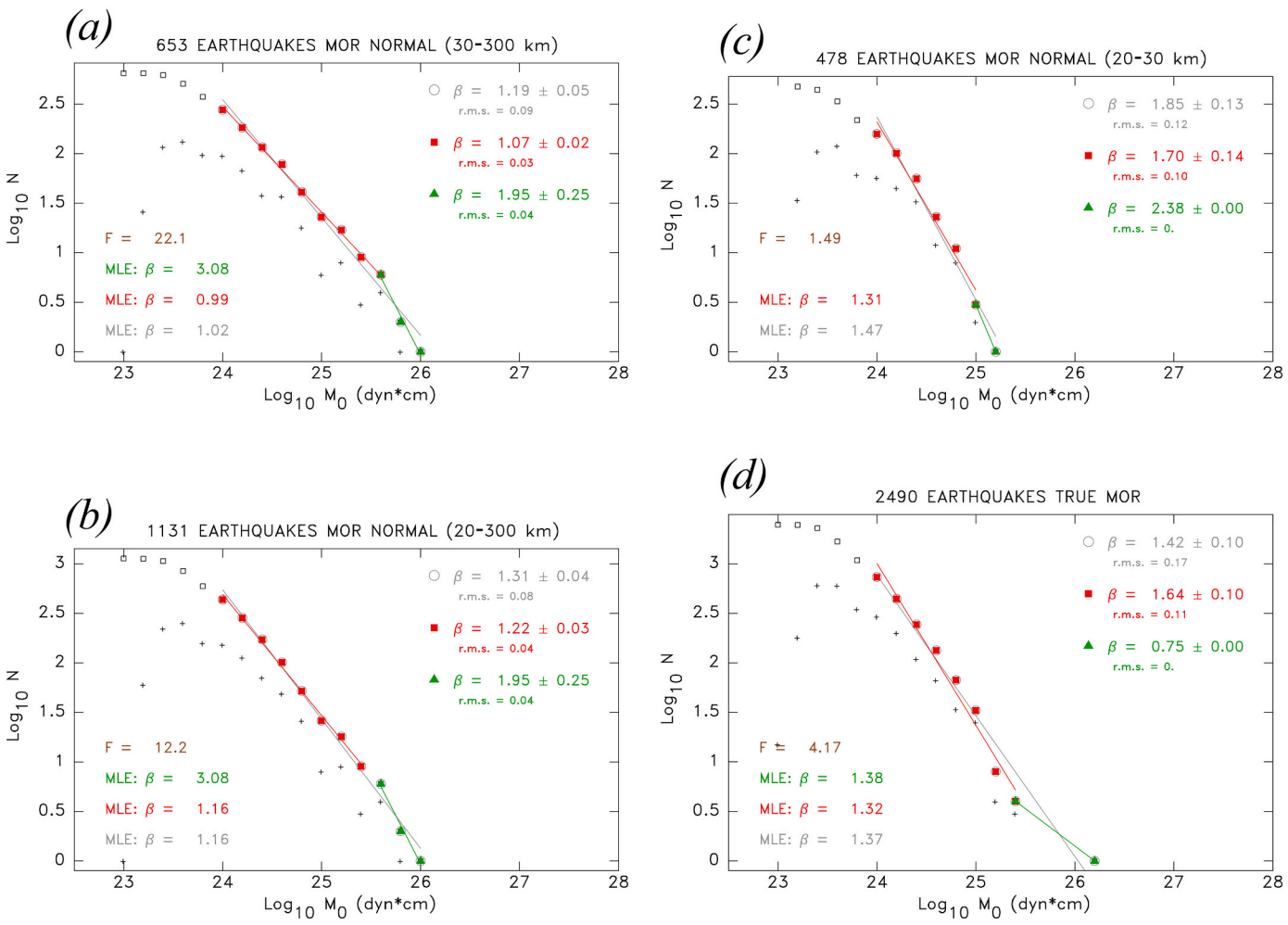

Fig. 13. Frequency-size relations for normal faulting intraplate oceanic earthquakes in the vicinity of mid-oceanic ridges. Symbols as in Fig. 1. Events are selected *(a)* between 30 and 300 km of a ridge segment; *(b)* between 20 and 300 km; *(c)* between 20 and 30 km; and for reference *(d)* within 20 km of the plate boundary (interplate events). See text for details.

seismogenic zone ($D = 3$; $\lambda = 1/3$), a model supported by the fact that the largest event in the regular population ($M_0 = 3.1 \times 10^{25}$ dyn*cm; Norwegian Sea, 2012) scales at only 8 km in fault width (Geller, 1976), thus remaining below the initiation of saturation. A single larger event ($M_0 = 1.4 \times 10^{26}$ dyn*cm) could suggest the initiation of saturation, but no conclusion can realistically be proposed on its basis alone; also, it took place in 2001 north of the Eltanin Fracture Zone, in an area where the Plate Tectonics framework may be evolving (Beutel and Okal, 2003).

6.3. Far away from ridges

"True" oceanic earthquakes then revert to the behavior of their worldwide counterparts (mostly interplate), with $\beta = 2/3$ (Fig. 12). Our results, which update those of Okal and Sweet (2007), indicate that these earthquakes take place on two-dimensional faults ($D = 2$), which are generally interpreted as representing zones of weakness in the plate, inherited from the fragmentation of spreading along transform fault segments (Sykes, 1978; Okal, 1983). We note, however, that this association with bathymetric features is highly variable, as discussed in the Pacific Ocean by Wysession et al. (1991).

Because of the thin nature of the intraplate seismogenic zone, controlled by its thermal evolution (Bergman and Solomon, 1984; Wiens and Stein, 1984), saturation will occur at lower moments than for the global population. The lone event (04 December 2015; Antarctic plate) in our dataset larger than in Okal and Sweet's (2007) could suggest the initiation of saturation under the *W*-model (Scholz, 1982) around 3×10^{26} dyn*cm, which would scale to 19 km in fault width, not an improbable figure for the average limit of a thermally controlled seismic zone. As detailed by Andrews et al. (2020), this earthquake is indeed remarkable for its size and hypocentral depth (34 km according to these authors, but between 16 and 35 km from other sources); the GlobalCMT centroid depth (29 km) locates on the 750°C isotherm, which is an acceptable value for the limit of the seismogenic zone (Wiens and Stein, 1984). We have verified that its energy-to-moment parameter (Newman and Okal, 1998), $\Theta = -5.23$, suggests neither slowness nor briskness in its source.

6.4. As the plate approaches subduction

Within 300 km of the plate boundary, "outer rise" seismicity becomes controlled by bending stresses. At small moments, it follows a classical distribution ($\beta \approx 2/3$), advocating rupture on pre-existing faults (Fig. 11). However, saturation then takes place under the *L*-model ($\beta \approx 1/2$), with the elbow moment poorly determined, suggesting that it could vary in different regions. Under that model (Scholz, 1982), seismic slip keeps growing with fault length, which allows for very large outer rise earthquakes (principally normal faulting) capable of generating exceptional tsunami run-up in the near-field, where amplitudes are directly related to fault slip rather than to seismic moment as in the far field (Okal and Synolakis, 2004). A typical example in this respect is the Showa Sanriku earthquake of 02 March 1933, at 7×10^{28} dyn*cm the largest normal faulting outer rise event ever recorded (Okal et al., 2016),

whose tsunami reached 29 m at Iwate. However, this argument remains qualitative, since the 1933 event and many of the larger outer rise earthquakes (07 March 1929; 30 March 1965) predate digital networks, and thus could not be included in the present study.

6.5. In the shallowest portions of the slab

Between 100 and 200 km, intraplate earthquakes again feature a distribution similar to that of the global dataset of shallow events, with $\beta = 2/3$ at low moments and $\beta = 1$ at larger ones (Fig. 2*b*). This behavior supports the concept of seismicity taking place on a system of faults, presumably inherited from the fractured lithospheric plate, as generally proposed by Boneh et al. (2019). The lower elbow moment, as compared with shallow (mostly interplate) earthquakes, simply illustrates the reduced width of the seismogenic zone, smaller than along the slab interface where dip angles are generally low, allowing for an extension of the seismic contact along the slab.

In this range of depths, Florez and Prieto (2019) recently suggested that in those slabs featuring double seismic zones, the upper layer (USL) exhibits a higher *b*-value than the lower one (LSL), with the difference in *b*-value increasing with the age of the subducting material, from a typical value of 0.15 units for young lithosphere (*e.g.*, Central and South America) to as much as 0.3 units in the coldest one (Tonga). However, their analysis suffers from using body-wave magnitudes m_b rather than seismic moments, as well as from the use of the MLE algorithm. In this context, we extracted from their original dataset of 2676 earthquakes those with published GlobalCMT solutions (1183 USL and 455 LSL), and applied our standard algorithm to the two subsets. This confirms a slight difference, but with the USLs actually showing a *higher* $\beta = 0.61$, *vs.* 0.71 (LSL), for $M_0 \leq 10^{26.5}$ dyn*cm, both numbers in good agreement with our world-wide regressed values at the relevant depths (15–300 km).

Those differences in β are reduced when further separating the two regions highlighted on Fig. 4 of Florez and Prieto (2019), namely Tonga ($\beta = 0.75$ (USL, 131 events) *vs.* 0.71 (LSL, 80 events)), and Central/South America ($\beta = 0.54$ (USL, 157 events) *vs.* 0.61 (LSL, 130 events)); note, in particular, the opposite trends in the two regions. In addition to the use of the MLE method, their results could be biased by that of body-wave magnitudes; we note in particular the presence in Florez and Prieto's (2019) dataset of several events with $m_b \geq 7$, suggesting a departure from scaling laws which predict saturation around $m_b = 6.0$ (Geller, 1976; Okal, 2019). As discussed by Okal and Romanowicz (1994), differences in the structural parameters controlling the relation between m_b and M_0 (*e.g.*, stress drops), or the conditions of saturation (*e.g.*, dimensions of the seismogenic material) could create artifacts in *b*-values derived from m_b populations in geologically different provinces.

Along similar lines, Kita and Ferrand (2018) relocated more than 12,000 earthquakes under Northern Honshu (Tohoku) and Hokkaido to refine the geometry of the local double seismic zones, and argued for a complex pattern of variations in *b*-values, with higher values in the upper zone than in the lower one in Hokkaido (0.98 *vs.* 0.86), but the opposite in the Tohoku province (0.86 *vs.* 0.96), with the Tohoku values themselves suffering from lateral and temporal variations. This intriguing situation may be affected by several factors, including the use of the MLE algorithm, which emphasizes the smallest events (see Section 3), and could thus be biased by local variations in detectability (including between the upper and lower zones) among the smallest earthquakes in the populations considered. Also, Kita and Ferrand (2018) use the local M_{JMA} magnitude scale, which at the very low magnitudes making up the bulk of their dataset would be in the nature of a high-frequency local magnitude M_L, which would exacerbate the problems described in this context by Okal and Romanowicz (1994). Unfortunately, we were unable to gather appropriate datasets in the Japanese double seismic zones in order to run an independent β-value study based on teleseismically derived seismic moments.

In short, seismicity in this depth range appears to take place on faults ($D = 2$) inherited from oceanic lithosphere, and in agreement with models of dehydration embrittlement (Boneh et al., 2019). It is, however, impossible to draw conclusions applicable globally regarding *b*-values in double seismic zones, especially given the degree of spatial and temporal variability reported by Kita and Ferrand (2018), and therefore it is probably futile to interpret slight differences on the order of 0.1 to 0.2 units in *b* in terms of variations in the structural parameters controlling seismogenesis.

There remains the intriguing observation that the systems of faults hosting outer rise and shallow intraslab earthquakes saturate differently in the two environments: along the *L*-model in the former, and along the *W*-model in the latter. While this is well documented from Figs. 2*b* and 11, the origin of this situation remains unclear. We note that the stress released in outer rise events is of a local nature, since it expresses the bending of the plate as it approaches the subduction, in contrast with stresses coherent on a larger scale both inside the oceanic plate ("true" intraplate events, Fig. 12) and deeper in the slab (Fig. 2*b*). Such bending events may be characterized by high stress drops, and we have verified that the ten largest outer-rise earthquakes ($M_0 > 10^{26}$ dyn*cm, hence beyond the elbows on Fig. 11) have slowness parameters Θ significantly larger (-4.42 ± 0.18) than found by Saloor and Okal (2018) for intermediate earthquakes (-4.81 ± 0.25 and -4.77 ± 0.24 between 80 and 135 km, and 135 and 300 km, respectively). In summary, the population of shallow intermediate events (100–200 km) seem to have more in common with "true" oceanic intraplate earthquakes (even though they can grow to much higher moments) than with those taking place right before the initiation of subduction (the so-called "outer-rise" events). These results would support the concept of shallow intraslab seismicity occurring through reactivation of pre-existing fractures upon dehydration (Ranero et al., 2003; Boneh et al., 2019), with the intense outer-rise seismicity appearing as a parenthesis in the history of the plate, which releases local bending stresses of a clearly different nature.

6.6. Between depths of 200 and 400 km

The general level of seismicity in the slabs reaches a minimum, but our results fail to document a definitive change in the frequency-size relationships, with β-values remaining close to 2/3. The major difference with shallower bins is the absence of a demonstrable elbow in the distribution, which could reflect undersampling at large moments in this range of reduced activity. While dehydration embrittlement has generally been proposed as a mechanism of seismogenesis for intermediate-depth earthquakes (Green and Houston, 1995; Kirby et al., 1996a), a detailed study in South America has shown that the level of seismicity, especially below 200 km, is not directly correlated with volcanism, a probable reflection of subtle lateral differences in temperature profiles (Chen et al., 2001).

An important result of our studies remains the absence of discernable changes in behavior at 300 km, thus underscoring the artificial nature of this traditional boundary between intermediate and deep earthquakes, whose origin is rather complex. It would seem that Wadati (1928, 1934) first proposed a boundary at 200 km, based on a correlation between intermediate shocks and active volcanism, which was visionary at the time. Gutenberg and Richter (1938) later deepened it to 250 km by considering in a broader sense "Tertiary tectonic activity". Finally, the boundary was moved to 300 km in their next paper (Gutenberg and Richter, 1939), allowing a separation into more "clearly distinguishable geographical groups", and that figure was then kept in all three editions of *Seismicity of the Earth* (Gutenberg and Richter, 1941, 1949, 1954), and

subsequently enshrined by the geophysical community. That final boundary between intermediate and deep events expressed a couple of phenomenological observables, namely the strong low in seismic activity starting at 300 km, and the bimodal distribution of maximum depths among subduction zones, few if any of which fall in the 300–500 km depth interval, as later documented, *e.g.*, by Kirby et al. (1991), Fig. 10).

However, given the state of knowledge of mineral physics in the late 1930s, the 300-km boundary obviously could not be justified on the basis of any interpretation of the origin of seismogenesis at depth. In this context, it would seem more appropriate to relocate it to a greater depth featuring a major evolution in the mineralogical properties of the mantle.

6.7. Below 400 km

The slab penetrates the transition zone and the process of transformational faulting in olivine remaining metastable in that relatively cold environment becomes possible (Kirby et al., 1996b).

In very general terms, our results below 500 km, where the rate of seismicity increases significantly, support the model proposed by Okal and Kirby (1995), namely a three-dimensional seismogenic zone undergoing a two-stage saturation. In particular, the increased population of larger earthquakes in our Tonga dataset suggests a third segment with a steeper β-value, which was missing from Okal and Kirby's (1995) study due to undersampling at large moments.

However, an interesting observation is that the transition to this regime takes place differently in Tonga, where it does not start until 500 km, and in the other subduction zones, where it is present in the 400–500 km bin. While we do not have a simple interpretation of this disparity, it is probably related to the extreme thermal parameter ($\Phi \approx 17{,}000$ km) of the Tonga slab.

Any interpretation of these observations must be sought in the context of the olivine → wadsleyite phase transformation, which delimits the top of the so-called transition zone, at a depth of 410 km in unperturbed mantle. Its Clapeyron slope of 34 MPa/K (Bina and Helffrich, 1994; Akaogi et al., 2007) translates into an upward deflection of 10 km per 100 K, expected to reach as much as 60 km inside a "regular" slab with a thermal parameter of 7000 km, or in its immediate vicinity as observed, *e.g.*, by Collier and Helffrich (2001), and even higher in the much colder Tonga slab, especially in its Northern segment, where efforts at documenting and interpreting similar deflections have been less conclusive and even controversial (Tibi and Wiens, 2005; Helffrich, 2005).

Under the model of transformational faulting, seismogenesis requires the presence of both metastable material (in this case, olivine), and a field of stresses to initiate the rupture. We refer, *e.g.*, to Kirby et al. (1996b) for a detailed mapping of the domain of metastable olivine, which obviously extends down from the depth of stable transformation, including any deflection, *i.e.*, 350 km in typical subduction zones, and possibly shallower in Tonga. Very young and/or slow slabs may be too warm for metastability, leading to the cessation of seismicity around 300 km, even though the slab may be present deeper, as detected by seismic tomography (*e.g.*, in Sumatra). Regarding stresses, the "parachute" model, suggested as early as Bassett (1979), expresses the buoyancy of the metastable olivine with respect to the surrounding mantle (which has transformed to denser wadsleyite), in contrast to the negative buoyancy expected from the simple effect of colder temperatures in the slab; such lateral variations in buoyancy create large stresses (Yoshioka et al., 1997), leading to intense seismicity generated by transformational faulting, especially deeper in the slab where the metastable material does not fill the entire slab (Kirby et al., 1996b, Fig. 9). However, in colder and faster slabs, and above 410 km, the metastable tongue is surrounded by mantle olivine of comparable (actually slightly greater) density, the parachute disappears, and with it the localized stresses. This model could explain the absence of significant seismicity in the 300–400 km depth bin.

Finally, in Tonga, while the lower temperatures help preserve a large domain of metastable olivine, thus increasing the potential for seismogenesis, they may adversely affect the kinetics of transformational faulting and thus retard the initiation of abundant seismicity until greater depths where the temperature is higher.

6.8. A discussion in the context of recent results

We compare here our results and interpretations with those of Zhan (2017), and analyze in detail differences between the two studies. In simple terms, Zhan (2017) proposes a dual-mechanism hypothesis in which deep earthquakes can rupture within the metastable olivine wedge of subducting slabs via transformational faulting (primarily at low moments), but also outside the wedge via dynamic shear banding and/or shear melting (mostly at high moments). The resulting frequency-size regimes for these two mechanisms are dictated by the size of the metastable wedge, itself controlled by the thermal structure of the subducting slab.

While the dataset used by Zhan (2017) is *a priori* identical to ours (but for the obvious inclusion of 2017–2020 data in the present study), several aspects of his algorithm differ significantly.

● *A different depth binning*

Zhan (2017) initially uses the coarse characterization of earthquakes as "intermediate" and "deep", with bounds placed at 70 and 300 km, this last partition being relatively arbitrary, as discussed above. By contrast, we have opted, both in Okal and Kirby (1995) and in the present study, for a systematically finer depth resolution with 100-km bins. In the case of "intermediate" earthquakes, this allows us to separate environments ($h \leq 200$ km) where intense dehydration is responsible for the generation of arc volcanism (*e.g.*, Ringwood, 1974), from the deeper layer (200–300 km) where the seismic budget strongly decreases with depth. At greater depths, our finer binning also allows the separation of the 300–400 km zone, which similarly features population statistics differing from the next deeper bin.

Zhan (2017) later separates the classical "deep" group at the 500–km depth threshold; given the general trends in seismicity with depth (except in the case of the Mariana-Bonin Trench), there is, expectedly, very little difference between his results for 300–700 and 500–700 km, the former population being overwhelmingly dominated by the latter. Note that the depth bins used by Zhan (2017) do not allow the separate study of the zone of reduced seismicity, from 200 to 400 km. We have shown in Section 4.3 that this zone has properties differing from those of both the shallower and deeper bins.

● *A different regional outlook*

By contrast with his coarser depth binning, Zhan (2017) individualizes six geographic zones ranked according to their thermal parameter Φ (Kirby et al., 1991, 1996b) (we note that regions with no or few deep earthquakes (>300 km), such as the Aleutians, the Solomons, Vanuatu, and the Aegean are excluded from this regionalization, despite their abundant intermediate depth populations). While this approach is legitimate, it can suffer from the inherent inhomogeneity in Φ in the case of extended subduction zones spanning provinces with varying tectonic parameters, such as South America, where the seismic and volcanic properties feature lateral heterogeneity correlated with variation in slab dip (Chen et al., 2001), and where a complex episode of ridge jumping in

the Cretaceous significantly altered the thermal parameter (Engebretson and Kirby, 1992), to the extent that the true properties of the slab at depth may be misrepresented by those of the presently subducting lithosphere. Similarly, the East Indonesian dataset earmarked by Zhan (2017) as a runner-up to Tonga in terms of a large thermal parameter Φ, relates to a mixture of complex regions featuring a reversal of subduction polarity (northwards in the North Australian Basin, southwards in the Flores Sea) and a mixture of Eocene-to-Neogene crust subducting in various parts of the Banda Sea (*e.g.*, Hamilton, 1979; Honthaas et al., 1998; Hinschberger et al., 2001), where the present tectonic regime is in places younger than the age of the deepest section of the slabs. It is difficult, under these conditions, to characterize East Indonesia with a single, let alone accurate parameter Φ.

Rather, as detailed in Appendix B, we elected to earmark only the Tonga subduction system, given its exceptional convergence rate (up to 20 cm/yr at its northern end leading to an unparalleled value of Φ, on the order of 17,000 km), and its abundant seismicity which allows significant populations, even using 100-km bins.

In the shallowest of his depth bins (70–300 km), Zhan (2017) reports *b*-values computed on moment magnitudes essentially equal to 1, equivalent to $\beta \approx 2/3$, with no regional signal. This value agrees with our results for the low-moment segments of our 100–200 km bin and with the one-segment regression of the 200–300 km one. However, Zhan (2017) does not consider the change of slope at higher moments already proposed by Okal and Kirby (1995) and confirmed here by our *F*-test studies (*e.g.*, Fig. 2*b*).

At the greatest depths ($h \geq 500$ km), Zhan (2017) documents a general increase in *b*-value with thermal parameter, and interprets this result in the context of a change of frequency-size distributions at larger magnitudes. For this purpose, and probably on account of the limited size of the regional populations, Zhan (2017) reverts to an approach paralleling ours, regrouping four non-Tonga subduction zones and comparing their distributions with those in Tonga. He then argues that Tonga features a largely "business as usual" distribution with $D = 2$ and $\lambda = 1/3$ ($n = 1/\lambda = 3$ in his notation), leading to $\beta = 2/3$ or $b = 1$. By contrast, the so-called "warm" slabs featuring a lower thermal parameter Φ would involve a different mechanism of seismogenesis, nucleating in a wedge of metastable olivine but then propagating outside it, with a fractal dimension $D = 1$ but still $n = 3$, leading to $\beta = 1/3$ or $b = 1/2$ for the population of smaller events below the elbow which he identifies at $M_w = 6.5$ ($10^{25.8}$ dyn*cm). The possibility of a rupture propagating outside the wedge of metastable olivine was first documented in the laboratory by Green et al. (1992); this certainly renders it a physically plausible phenomenon, albeit not necessarily a universal explanation of deep seismicity, as discussed below. In order to explain the higher *b*-value beyond the elbow, Zhan (2017) proposes reverting to $D = 2$, but keeping $n = 3$ ($\lambda = 1/3$).

While Zhan's (2017) model is indeed imaginative and deserves attention, we identify the following problems. First and foremost, the model assumes $n = 3$ ($\lambda = 1/3$) under all conditions (no saturation in width and slip), when for shallow earthquakes the well-documented presence of an elbow is universally explained by a variation in λ caused by saturation. In particular, it seems difficult to argue for a change to $D = 1$ (meaning that the seismogenic zone can grow in only one dimension) but to keep $\lambda = 1/3$ (meaning that all three factors in M_0, including width, keep growing). Thus, it would seem more plausible to explain similar elbows in the population of deep earthquakes by a change in λ, accompanying one in *D*.

Next, the slopes proposed by Zhan (2017) for the non-Tonga 500–700 km range ($b = 1/2$ and 1, or $\beta = 1/3$ and 2/3) differ from those proposed here in the 500–600 km bin ($\beta = 1/2$ and 1, in line with the model of Okal and Kirby (1995)). We have verified that this discrepancy results from different population distributions above and below 600 km being combined into a single dataset; we recall here that Okal and Kirby (1995) documented that merging two earthquake groups with different population statistics could build a dataset with the appearance of a simple frequency-moment relationship, while neither of its parts actually followed it. Note in particular that the deepest part of subduction zones ($h \geq 600$ km) is characterized by regional heterogeneity, as the interaction between the slab and the bottom of the transition zone occasionally (but not always) leads to sagging (*e.g.*, Goes et al., 2017), and hence to a departure from the simple geometry of the metastable olivine wedge, which controls the saturation of the dimension of earthquake sources. This effect was mentioned by Okal et al. (2018) to explain the exceptional size of the 2013 Sea of Okhotsk event. It could then be unwarranted to draw conclusions from the properties of an inhomogeneous dataset including all depths from 500 to 690 km, when processed as a single entity.

Thus, the discrepancies between our results and Zhan's (2017) are probably attributable to different approaches in subdividing an obviously heterogeneous dataset: finer depth binning and coarser regionalization in our case, *vs.* the opposite in Zhan's (2017). Clearly, a fine binning both by depth and region would be preferable, but is made impossible by the limited size of the resulting groups, which would be too small for reliable processing; this situation will probably remain unchanged for at least a couple of decades.

In summary, our results seem more consistent with Okal and Kirby's (1995) model: indeed, they provide support for these authors' proposed three-tier framework, since the large-moment $\beta = 1$ regime in Tonga (which they could not identify due to a paucity of large-moment, deep earthquakes) appears in the 500–600 km depth bin and is validated by an *F*-test.

Declaration of Competing Interest

None

Acknowledgements

We thank Craig Bina, Suzan van der Lee, Michael Witek, and numerous others for helpful discussions and input. Seth Stein provided insight into the *F*-test methodology. We are grateful to Gavin Hayes for coaching us on the use of the Slab2 model. This work was supported at Northwestern University by a Weinberg College of Arts and Sciences undergraduate research grant to J.P.T., and constituted a significant portion of his undergraduate thesis. J.P.T. also acknowledges support from the National Science Foundation Graduate Research Fellowship Program, under Grant DGE 17-46045. The paper was improved by the comments of two anonymous reviewers.

Appendix A. Sensitivity of the MLE method to fluctuations in average magnitude

When computed over a finite interval of magnitudes, $\{M_d, M_u\}$ (for "down" and "up"), the average magnitude of a population scaling with a Gutenberg-Richter slope *b* will be given by

$$< M >= \frac{M_d - M_u 10^{-b(M_u - M_d)}}{1 - 10^{-b(M_u - M_d)}} + \frac{\log_{10} e}{b} \tag{A1}$$

which replaces (5), to which it obviously reduces when $M_u \to \infty$. Conversely, this equation can be used to solve numerically for *b* once an average magnitude $<M>$ is obtained.

We examine here the problem of the robustness of the final result *b*, when small fluctuations can affect the value of $<M>$. We are motivated by the fact that magnitudes or moment values obtained from catalogs

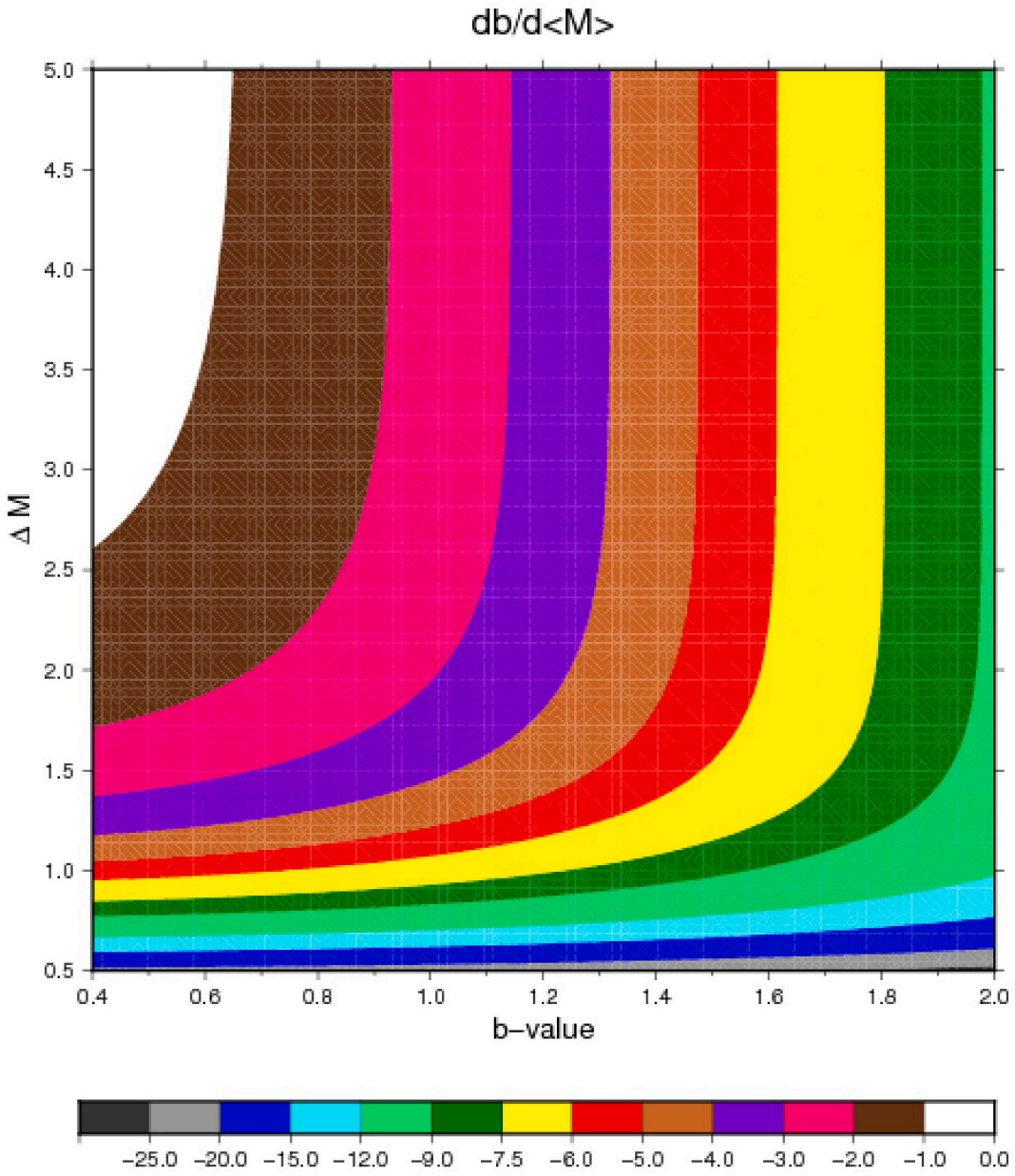

Fig. A1. Sensitivity of MLE-computed b-value to fluctuations in average magnitude $<M>$, expressed as the derivative $db/d<M>$ obtained from Eq. (A3), contoured as a function of true b-value and width of magnitude window ΔM. See Appendix A for details.

are never exact, but rather always rounded up, most often to 0.1 unit of magnitude or two significant digits for a moment, this procedure being *de facto* equivalent to binning (Bender, 1983). As a result, and depending on the computational details, notably to handle earthquakes with sizes at the edges of the sampled windows (Marzocchi and Sandri, 2003), we have found that estimates of M can fluctuate by about 0.1 units of magnitude (or of $\log_{10}M_0$).

The effect on the resulting b-value can be estimated by differentiating (A1) to obtain the derivative $\dfrac{db}{d<M>}$; we first obtain its inverse

$$\frac{d<M>}{db} = (\ln 10)\left[\frac{(\Delta M)^2 10^{-b\Delta M}}{\left(1-10^{-b\Delta M}\right)^2} - \frac{(\log_{10}e)^2}{b^2}\right] \tag{A2}$$

and then

$$\frac{db}{d<M>} = \frac{\ln 10}{(\ln 10)^2 \dfrac{(\Delta M)^2 10^{-b\Delta M}}{\left(1-10^{-b\Delta M}\right)^2} - \dfrac{1}{b^2}} \tag{A3}$$

This function of b and of the width $\Delta M = M_u - M_d$ of the magnitude window studied is contoured on Fig. A1. As expected, the results indicate that b becomes extremely sensitive to fluctuations in measured $<M>$ when the width of the sampling window, ΔM, decreases to and below one unit of magnitude. For a typical b-value of 1, and with $\Delta M \geq 2$, the derivative is practically constant, meaning that a fluctuation of 0.1 unit in $<M>$ will result in a variation of approximately 0.25 unit of b. If ΔM is reduced to 1 unit, this number is essentially doubled. In practice, this means that the MLE method cannot resolve b-values to better than about 0.25 unit, even when $\Delta M \geq 2$.

It is easy to show that an exactly similar plot (and hence similar

conclusions) would be obtained when considering moments M_0 rather than magnitudes, by reading the abscissa as β-values, and the ordinates as directly $\log_{10}(M_0^u/M_0^d)$; the contoured quantity would then be $[d\beta/d(<\log_{10}M_0>)]$.

Appendix B. The unique character of the Tonga subduction zone

We discuss here the unique properties of the "Tonga" subduction zone (hereafter TSZ), which justify considering it separately from all other Wadati-Benioff subduction systems for our analyses of frequency-size relationships. For simplicity, and as mentioned in the main text, we define this region as bounded by latitudes 40°S and 10°S and longitudes 175°E and 175°W. However, the maximum depth of seismicity, as well as its total budget, decrease sharply South of 26°S, so that the entire dataset of deep "Tonga" events reflects mostly the properties of the Tonga Islands and Northern Kermadec provinces.

We recall that the TSZ features the highest documented convergence rates, varying from 16 cm/yr at 22°S to as much as 24 cm/yr at 16°S (Bevis et al., 1995). Despite the lack of precise measurements of the age of the subducting lithosphere generated during the Cretaceous magnetic quiet interval, its thermal parameter Φ (Kirby et al., 1991) can be estimated to reach 17,000 km in the North, resulting in an exceptionally cold environment inside the slab. This will have consequences on the extent and properties of the zone of olivine metastability, in the framework of seismogenesis due to transformational faulting (Kirby et al., 1996b), but also at lesser depths on the process of dehydration embrittlement, thought to be responsible for intermediate-depth seismicity, which could extend beyond 300 km in Tonga, as discussed recently by Wei et al. (2017).

In addition, the distribution of seismicity inside the TSZ displays remarkable features. We recall that over the past 20 years, the expansion of seismic networks, the development of laterally heterogeneous velocity models, and progress in automatic identification and modeling of depth phases (Engdahl et al., 2020) have resulted in a considerable improvement in three-dimensional relocation of deep sources, including for historical events. The resulting datasets, *e.g.*, the ISC-EHB, USGS Centennial and ISC-GEM catalogues (Weston et al., 2018; Engdahl et al., 1998; International Seismological Center, 2020), provide a more precise and hopefully more accurate insight on the fine scale geometry of seismic provinces, especially in WBZs. In most subduction zones, the emerging picture of the seismogenic zone is that of smoothly varying curvi-planar surfaces, not exceeding a few tens of km in thickness, with the possibility, especially at intermediate depths, of two (or exceptionally more) such features separated by a seismically quiescent volume (the so-called "double seismic zones") (*e.g.*, Brudzinski et al., 2007; Kita and Ferrand, 2018; Florez and Prieto, 2019). By contrast, in the TSZ, the spatial distribution of deep earthquakes departs significantly from such smoothly varying geometries, illustrating different dynamics for slab descent and stresses. As already discussed by Okal and Kirby (1998), and later more widely documented in the above datasets of improved relocations, such departures comprise (A) outboard events and earthquake clusters located above the main WBZ; (B) sharp kinks in the WBZ; (C) lateral offsets of the WBZ, and a resultant doubling of the zone, thought to be a consequence of large shear displacements; and (D) deep earthquakes in flat-lying "sagging" segments of the WBZ making up so-called "stagnant" or "recumbent" slabs, that typically reflect fast trench migration (*e.g.*, around 18°S and 20–21°S), or a recent radical evolution of the orientation of subduction, such as under the deep Fiji Basin (Hamburger and Isacks, 1987; Okal and Kirby, 1998; Chen and Brudzinski, 2001). These features are documented on cross-sections of the Tonga-Kermadec subduction zone published online by the International Seismological Center (2020).

It is clear that the above features, in particular (B), (C) and (D), result in a systematic deformation (mostly, in an increase) of seismogenic zones, which can significantly affect the growth and/or saturation of earthquake sources within them. In addition, as documented by Okal and Kirby (1998) and confirmed by later seismicity as catalogued under the GlobalCMT project (Ekström et al., 2012), the relevant events do not share the orientation of focal mechanism expected at the bottom of subduction zones, *i.e.*, down-dip compression. Finally, on the basis of detailed tomography and waveform modeling, Brudzinski and Chen (2000, 2003) have concluded that, in addition to strong temperature anomalies, the structure of outboard or sagging slab elements in the TSZ require petrological heterogeneities, which could consist of metastable material. In this context, the properties of the TSZ are clearly extremely singular, and justify isolating it from other subduction zones for the study of its frequency-size characteristics.

References

Abramowitz, M., Stegun, I.A., 1964. Handbook of Mathematical Functions with Formulas, Graphs, and Mathematical Tables, Chapters 6 and 26. U.S. Government Printing Office, Dover, New York.

Akaogi, M., Takayama, H., Kojitani, H., Kawaji, H., Atake, T., 2007. Low-temperature heat capacities, entropies and enthalpies of Mg_2SiO_4 polymorphs, and $\alpha-\beta-\gamma$ and post-spinel phase relations at high pressure. Phys. Chem. Miner. 34, 169–183. https://doi.org/10.1007/s00269-006-0137-3.

Aki, K., 1965. Maximum likelihood estimate of b in the formula log $N = a$ - bM and its confidence limits. Bull. Earthq. Res. Inst. Tokyo Univ. 43, 237–238.

Andrews, R., Rajendran, K., Rao, N.P., 2020. The 4 December 2015 M_w 7.1 normal-faulting Antarctic plate earthquake and its seismotectonic implications. Bull. Seismol. Soc. Am. 110, 1090–1100. https://doi.org/10.1785/0120190249.

Bassett, W.A., 1979. The diamond cell and the nature of the earth's mantle. Annu. Rev. Earth Planet. Sci. 7, 357–384. https://doi.org/10.1146/annurev.ea.07.050179.002041.

Båth, M., 1981. Earthquake magnitude — recent research and current trends. Earth Sci. Rev. 17, 315–398. https://doi.org/10.1016/0012-8252(81)90014-3.

Bender, B., 1983. Maximum likelihood estimation of b values for magnitude grouped data. Bull. Seismol. Soc. Am. 73, 831–851.

Bergman, E.A., Solomon, S.C., 1984. Source mechanisms of earthquakes near mid-ocean ridges from body waveform inversion: implications for the early evolution of oceanic lithosphere. J. Geophys. Res. Solid Earth 89, 11415–11441. https://doi.org/10.1029/JB089iB13p11415.

Beutel, E.K., Okal, E.A., 2003. Strength asperities along oceanic transform faults: a model for the origin of extensional earthquakes on the Eltanin transform system. Earth Planet. Sci. Lett. 216, 27–41. https://doi.org/10.1016/S0012-821X(03)00484-9.

Bevis, M., Taylor, F.W., Schutz, B.E., Recy, J., Isacks, B.L., Helu, S., Singh, R., Kendrick, E., Stowell, J., Taylor, B., Calmantli, S., 1995. Geodetic observations of very rapid convergence and back-arc extension at the Tonga arc. Nature 374, 249–251. https://doi.org/10.1038/374249a0.

Bina, C.R., Helffrich, G., 1994. Phase transition Clapeyron slopes and transition zone seismic discontinuity topography. J. Geophys. Res. Solid Earth 99, 15853–15860. https://doi.org/10.1029/94JB00462.

Bird, P., 2003. An updated digital model of plate boundaries. Geochem. Geophys. Geosyst. 4 https://doi.org/10.1029/2001GC000252.

Boneh, Y., Schottenfels, E., Kwong, K., Zelst, I.v., Tong, X., Eimer, M., Miller, M.S., Moresi, L., Warren, J.M., Wiens, D.A., Billen, M., Naliboff, J., Zhan, Z., 2019. Intermediate-depth earthquakes controlled by incoming plate hydration along bending-related faults. Geophys. Res. Lett. 46, 3688–3697. https://doi.org/10.1029/2018GL081585.

Brudzinski, M.R., Chen, W.P., 2000. Variations in P wave speeds and outboard earthquakes: evidence for a petrologic anomaly in the mantle transition zone. J. Geophys. Res. Solid Earth 105, 21661–21682. https://doi.org/10.1029/2000JB900160.

Brudzinski, M.R., Chen, W.P., 2003. A petrologic anomaly accompanying outboard earthquakes beneath Fiji-Tonga: corresponding evidence from broadband P and S waveforms. J. Geophys. Res. Solid Earth 108, 2299. https://doi.org/10.1029/2002JB002012.

Brudzinski, M.R., Thurber, C.H., Hacker, B.R., Engdahl, E.R., 2007. Global prevalence of double Benioff zones. Science 316, 1472–1474. https://doi.org/10.1126/science.1139204.

Chapple, W.M., Forsyth, D.W., 1979. Earthquakes and bending of plates at trenches. J. Geophys. Res. Solid Earth 84, 6729–6749. https://doi.org/10.1029/JB084iB12p06729.

Chen, P.F., Bina, C.R., Okal, E.A., 2001. Variations in slab dip along the subducting Nazca Plate, as related to stress patterns and moment release of intermediate-depth seismicity and to surface volcanism. Geochem. Geophys. Geosyst. 2, 1054. https://doi.org/10.1029/2001GC000153.

Chen, W.P., Brudzinski, M.R., 2001. Evidence for a large-scale remnant of subducted lithosphere beneath Fiji. Science 292, 2475–2479. https://doi.org/10.1126/science.292.5526.2475.

Collier, J.D., Helffrich, G.R., 2001. The thermal influence of the subducting slab beneath South America from 410 and 660 km discontinuity observations. Geophys. J. Int. 147, 319–329. https://doi.org/10.1046/j.1365-246X.2001.00532.x.

Dixon, W.J., Massey Jr, F.J., 1969. Introduction to statistical analysis, 3rd ed. McGraw-Hill, New York.
Dziewonski, A.M., Chou, T.A., Woodhouse, J.H., 1981. Determination of earthquake source parameters from waveform data for studies of global and regional seismicity. J. Geophys. Res. Solid Earth 86, 2825–2852. https://doi.org/10.1029/JB086iB04p02825.
Ekström, G., Nettles, M., Dziewoński, A.M., 2012. The global CMT project 2004–2010: centroid-moment tensors for 13,017 earthquakes. Phys. Earth Planet. Inter. 200-201, 1–9. https://doi.org/10.1016/j.pepi.2012.04.002.
Engdahl, E.R., van der Hilst, R., Buland, R., 1998. Global teleseismic earthquake relocation with improved travel times and procedures for depth determination. Bull. Seismol. Soc. Am. 88, 722–743.
Engdahl, E.R., Giacomo, D.D., Sakarya, B., Gkarlaouni, C.G., Harris, J., Storchak, D.A., 2020. ISC-EHB 1964–2016, an improved data set for studies of earth structure and global seismicity. Earth Space Sci. 7 https://doi.org/10.1029/2019EA000897 e2019EA000897.
Engebretson, D., Kirby, S.H., 1992. Deep Nazca slab seismicity: why is it so anomalous. Eos, Trans. Amer. Geophys. Union 73 (43), 379 [abstract].
Florez, M.A., Prieto, G.A., 2019. Controlling factors of seismicity and geometry in double seismic zones. Geophys. Res. Lett. 46, 4174–4181. https://doi.org/10.1029/2018GL081168.
Freed, A.M., 2005. Earthquake triggering by static, dynamic, and postseismic stress transfer. Annu. Rev. Earth Planet. Sci. 33, 335–367. https://doi.org/10.1146/annurev.earth.33.092203.122505.
Frohlich, C., 1987. Aftershocks and temporal clustering of deep earthquakes. J. Geophys. Res. Solid Earth 92, 13944–13956. https://doi.org/10.1029/JB092iB13p13944.
Frohlich, C., Davis, S.D., 1993. Teleseismic *b* values; Or, much ado about 1.0. J. Geophys. Res. Solid Earth 98, 631–644. https://doi.org/10.1029/92JB01891.
Gardner, J.K., Knopoff, L., 1974. Is the sequence of earthquakes in Southern California, with aftershocks removed, Poissonian? Bull. Seismol. Soc. Am. 64, 1363–1367.
Geller, R.J., 1976. Scaling relations for earthquake source parameters and magnitudes. Bull. Seismol. Soc. Am. 66, 1501–1523.
Giardini, D., 1988. Frequency distribution and quantification of deep earthquakes. J. Geophys. Res. Solid Earth 93, 2095–2105. https://doi.org/10.1029/JB093iB03p02095.
Goes, S., Agrusta, R., van Hunen, J., Garel, F., 2017. Subduction-transition zone interaction: a review. Geosphere 13, 644–664. https://doi.org/10.1130/GES01476.1.
Green, H.W.I., Houston, H., 1995. The mechanics of deep earthquakes. Annu. Rev. Earth Planet. Sci. 23, 169–213. https://doi.org/10.1146/annurev.ea.23.050195.001125.
Green, H.W.I., Scholz, C.H., Tingle, T.N., Young, T.E., Koczynski, T.A., 1992. Acoustic emissions produced by anticrack faulting during the olivine spinel transformation. Geophys. Res. Lett. 19, 789–792. https://doi.org/10.1029/92GL00751.
Gutenberg, B., Richter, C.F., 1938. Depth and geographical distribution of deep-focus earthquakes. GSA Bull. 49, 249–288. https://doi.org/10.1130/GSAB-49-249.
Gutenberg, B., Richter, C.F., 1939. Depth and geographical distribution of deep-focus earthquakes (second paper). GSA Bull. 50, 1511–1528. https://doi.org/10.1130/GSAB-50-1511.
Gutenberg, B., Richter, C.F., 1941. Seismicity of the Earth. Geol. Soc. Am. Spec. Pap. 34, 1–125.
Gutenberg, B., Richter, C., 1949. Seismicity of the Earth and Associated Phenomena, 1 ed. Princeton University Press, Princeton, New Jersey.
Gutenberg, B., Richter, C., 1954. Seismicity of the Earth and Associated Phenomena, 2 ed. Princeton University Press, Princeton, New Jersey.
Hamburger, M.W., Isacks, B.L., 1987. Deep earthquakes in the Southwest Pacific: a tectonic interpretation. J. Geophys. Res. Solid Earth 92, 13841–13854. https://doi.org/10.1029/JB092iB13p13841.
Hamilton, W., 1979. Tectonics of the Indonesian Region. U. S. Geol. Surv. Prof. Pap. 1078, 1–345.
Hayes, G.P., Moore, G.L., Portner, D.E., Hearne, M., Flamme, H., Furtney, M., Smoczyk, G.M., 2018. Slab2, a comprehensive subduction zone geometry model. Science 362, 58–61. https://doi.org/10.1126/science.aat4723.
Helffrich, G., 2005. Trouble under Tonga? Nature 436, 637–638. https://doi.org/10.1038/436637a.
Hinschberger, F., Malod, J.A., Dyment, J., Honthaas, C., Réhault, J.P., Burhanuddin, S., 2001. Magnetic lineations constraints for the back-arc opening of the Late Neogene South Banda Basin (eastern Indonesia). Tectonophysics 333, 47–59. https://doi.org/10.1016/S0040-1951(00)00266-3.
Honthaas, C., Réhault, J.P., Maury, R.C., Bellon, H., Hémond, C., Malod, J.A., Cornée, J. J., Villeneuve, M., Cotten, J., Burhanuddin, S., Guillou, H., Arnaud, N., 1998. A Neogene back-arc origin for the Banda Sea basins: geochemical and geochronological constraints from the Banda ridges (East Indonesia). Tectonophysics 298, 297–317. https://doi.org/10.1016/S0040-1951(98)00190-5.
International Seismological Center, 2020. ISC-EHB Dataset. https://doi.org/10.31905/PY08W6S3.
Isacks, B., Molnar, P., 1971. Distribution of stresses in the descending lithosphere from a global survey of focal-mechanism solutions of mantle earthquakes. Rev. Geophys. 9, 103–174. https://doi.org/10.1029/RG009i001p00103.
Kagan, Y.Y., 2002. Seismic moment distribution revisited: I. Statistical results. Geophys. J. Int. 148, 520–541. https://doi.org/10.1046/j.1365-246x.2002.01594.x.
Kanamori, H., 1977. The energy release in great earthquakes. J. Geophys. Res. 82, 2981–2987. https://doi.org/10.1029/JB082i020p02981.
Kanamori, H., Anderson, D.L., 1975. Theoretical basis of some empirical relations in seismology. Bull. Seismol. Soc. Am. 65, 1073–1095.
Kirby, S.H., Durham, W.B., Stern, L.A., 1991. Mantle phase changes and deep-earthquake faulting in subducting lithosphere. Science 252, 216–225. https://doi.org/10.1126/science.252.5003.216.
Kirby, S., Engdahl, R.E., Denlinger, R., 1996a. Intermediate-depth intraslab earthquakes and arc volcanism as physical expressions of crustal and uppermost mantle metamorphism in subducting slabs. In: Subduction Top to Bottom, Amer. Geophys. Un. Geophys. Monogr. 96, pp. 195–214.
Kirby, S.H., Stein, S., Okal, E.A., Rubie, D.C., 1996b. Metastable mantle phase transformations and deep earthquakes in subducting oceanic lithosphere. Rev. Geophys. 34, 261–306. https://doi.org/10.1029/96RG01050.
Kita, S., Ferrand, T.P., 2018. Physical mechanisms of oceanic mantle earthquakes: comparison of natural and experimental events. Sci. Rep. 8, 17049. https://doi.org/10.1038/s41598-018-35290-x.
Lay, T., Ammon, C.J., Kanamori, H., Xue, L., Kim, M.J., 2011. Possible large near-trench slip during the 2011 M_w 9.0 off the Pacific coast of Tohoku earthquake. Earth Planets Space 63, 687–692. https://doi.org/10.5047/eps.2011.05.033.
Leith, A., Sharpe, J.A., 1936. Deep-focus earthquakes and their geological significance. J. Geol. 44, 877–917. https://doi.org/10.1086/624495.
Lundgren, P., Giardini, D., 1994. Isolated deep earthquakes and the fate of subduction in the mantle. J. Geophys. Res. Solid Earth 99, 15833–15842. https://doi.org/10.1029/94JB00038.
Luyendyk, B.P., Macdonald, K.C., 1977. Physiography and structure of the inner floor of the FAMOUS rift valley: observations with a deep-towed instrument package. GSA Bull. 88, 648–663. https://doi.org/10.1130/0016-7606(1977)88<648:PASOTI>2.0.CO;2.
Marzocchi, W., Sandri, L., 2003. A review and new insights on the estimation of the *b*-value and its uncertainty. Ann. Geophys. 46 https://doi.org/10.4401/ag-3472.
McNutt, S.R., 2005. Volcanic seismology. Annu. Rev. Earth Planet. Sci. 33, 461–491. https://doi.org/10.1146/annurev.earth.33.092203.122459.
Meade, C., Jeanloz, R., 1991. Deep-focus earthquakes and recycling of water into the earth's mantle. Science 252, 68–72. https://doi.org/10.1126/science.252.5002.68.
Minakami, T., 1974. Seismology of volcanoes in Japan. In: Civetta, L., Gasparini, P., Luongo, G., Rapolla, A. (Eds.), Developments in Solid Earth Geophysics. Elsevier. volume 6 of Physical Volcanology, pp. 1–27. https://doi.org/10.1016/B978-0-444-41141-9.50007-3.
Molnar, P., 1979. Earthquake recurrence intervals and plate tectonics. Bull. Seismol. Soc. Am. 69, 115–133.
Newman, A.V., Okal, E.A., 1998. Teleseismic estimates of radiated seismic energy: The E/M_0 discriminant for tsunami earthquakes. J. Geophys. Res. Solid Earth 103, 26885–26898. https://doi.org/10.1029/98JB02236.
Okal, E.A., 1983. Oceanic intraplate seismicity. Annu. Rev. Earth Planet. Sci. 11, 195–214. https://doi.org/10.1146/annurev.ea.11.050183.001211.
Okal, E.A., 2019. Energy and magnitude: a historical perspective. Pure Appl. Geophys. 176, 3815–3849. https://doi.org/10.1007/s00024-018-1994-7.
Okal, E.A., Kirby, S.H., 1995. Frequency-moment distribution of deep earthquakes; implications for the seismogenic zone at the bottom of slabs. Phys. Earth Planet. Inter. 92, 169–187. https://doi.org/10.1016/0031-9201(95)03037-8.
Okal, E.A., Kirby, S.H., 1998. Deep earthquakes beneath the Fiji Basin, SW Pacific: Earth's most intense deep seismicity in stagnant slabs. Phys. Earth Planet. Inter. 109, 25–63. https://doi.org/10.1016/S0031-9201(98)00116-2.
Okal, E.A., Romanowicz, B.A., 1994. On the variation of *b*-values with earthquake size. Phys. Earth Planet. Inter. 87, 55–76. https://doi.org/10.1016/0031-9201(94)90021-3.
Okal, E.A., Sweet, J.R., 2007. Frequency-size distributions of intraplate earthquakes. In: Stein, S., Mazzotti, S. (Eds.), Continental Intraplate Earthquakes: Science, Hazard and Policy Issues, Geol. Soc. Amer., Spec. Paper 425, pp. 59–72.
Okal, E.A., Synolakis, C.E., 2004. Source discriminants for near-field tsunamis. Geophys. J. Int. 158, 899–912. https://doi.org/10.1111/j.1365-246X.2004.02347.x.
Okal, E.A., Kirby, S.H., Kalligeris, N., 2016. The Showa Sanriku earthquake of 1933 March 2: a global seismological reassessment. Geophys. J. Int. 206, 1492–1514. https://doi.org/10.1093/gji/ggw206.
Okal, E.A., Saloor, N., Kirby, S.H., Nettles, M., 2018. An implosive component to the source of the deep Sea of Okhotsk earthquake of 24 May 2013: evidence from radial modes and CMT inversion. Phys. Earth Planet. Inter. 281, 68–78. https://doi.org/10.1016/j.pepi.2018.04.007.
Okazaki, K., Hirth, G., 2016. Dehydration of lawsonite could directly trigger earthquakes in subducting oceanic crust. Nature 530, 81–84. https://doi.org/10.1038/nature16501.
Pacheco, J.F., Scholz, C.H., Sykes, L.R., 1992. Changes in frequency–size relationship from small to large earthquakes. Nature 355, 71–73. https://doi.org/10.1038/355071a0.
Peacock, S.M., 2001. Are the lower planes of double seismic zones caused by serpentine dehydration in subducting oceanic mantle? Geology 29, 299–302. https://doi.org/10.1130/0091-7613(2001)029<0299:ATLPOD>2.0.CO;2.
Ranero, C.R., Phipps Morgan, J., McIntosh, K., Reichert, C., 2003. Bending-related faulting and mantle serpentinization at the Middle America trench. Nature 425, 367–373. https://doi.org/10.1038/nature01961.
Richter, C.F., 1935. An instrumental earthquake magnitude scale. Bull. Seismol. Soc. Am. 25, 1–32.

Ringwood, A.E., 1974. The petrological evolution of island arc systems. J. Geol. Soc. 130, 183–204. https://doi.org/10.1144/gsjgs.130.3.0183.
Roberts, N.S., Bell, A.F., Main, I.G., 2015. Are volcanic seismic *b*-values high, and if so when? J. Volcanol. Geotherm. Res. 308, 127–141. https://doi.org/10.1016/j.jvolgeores.2015.10.021.
Romanowicz, B., Rundle, J.B., 1993. On scaling relations for large earthquakes. Bull. Seismol. Soc. Am. 83, 1294–1297.
Rundle, J.B., 1989. Derivation of the complete Gutenberg-Richter magnitude-frequency relation using the principle of scale invariance. J. Geophys. Res. Solid Earth 94, 12337–12342. https://doi.org/10.1029/JB094iB09p12337.
Saloor, N., Okal, E.A., 2018. Extension of the energy-to-moment ratio Θ to intermediate and deep earthquakes. Phys. Earth Planet. Inter. 274, 37–48. https://doi.org/10.1016/j.pepi.2017.10.006.
Savage, J.C., 1969. The mechanics of deep-focus faulting. Tectonophysics 8, 115–127. https://doi.org/10.1016/0040-1951(69)90085-7.
Scholz, C.H., 1982. Scaling laws for large earthquakes: consequences for physical models. Bull. Seismol. Soc. Am. 72, 1–14.
Scholz, C.H., 2015. On the stress dependence of the earthquake *b* value. Geophys. Res. Lett. 42, 1399–1402. https://doi.org/10.1002/2014GL062863.
Schorlemmer, D., Wiemer, S., Wyss, M., 2005. Variations in earthquake-size distribution across different stress regimes. Nature 437, 539–542. https://doi.org/10.1038/nature04094.
Shi, Y., Bolt, B.A., 1982. The standard error of the magnitude-frequency b value. Bull. Seismol. Soc. Am. 72, 1677–1687.
Stauder, W., 1968. Mechanism of the Rat Island earthquake sequence of February 4, 1965, with relation to island arcs and sea-floor spreading. J. Geophys. Res. 73, 3847–3858. https://doi.org/10.1029/JB073i012p03847.
Stein, S., Gordon, R.G., 1984. Statistical tests of additional plate boundaries from plate motion inversions. Earth Planet. Sci. Lett. 69, 401–412. https://doi.org/10.1016/0012-821X(84)90198-5.
Stein, S., Okal, E.A., 2005. Speed and size of the Sumatra earthquake. Nature 434, 581–582. https://doi.org/10.1038/434581a.
Stein, S., Okal, E.A., 2007. Ultralong period seismic study of the December 2004 Indian Ocean earthquake and implications for regional tectonics and the subduction process. Bull. Seismol. Soc. Am. 97, S279–S295. https://doi.org/10.1785/0120050617.
Sykes, L.R., 1978. Intraplate seismicity, reactivation of preexisting zones of weakness, alkaline magmatism, and other tectonism postdating continental fragmentation. Rev. Geophys. 16, 621–688. https://doi.org/10.1029/RG016i004p00621.
Tafti, T.A., Sahimi, M., Aminzadeh, F., Sammis, C.G., 2013. Use of microseismicity for determining the structure of the fracture network of large-scale porous media. Phys. Rev. E 87, 032152. https://doi.org/10.1103/PhysRevE.87.032152.
Tibi, R., Wiens, D.A., 2005. Detailed structure and sharpness of upper mantle discontinuities in the Tonga subduction zone from regional broadband arrays. J. Geophys. Res. Solid Earth 110. https://doi.org/10.1029/2004JB003433.
Tréhu, A.M., Solomon, S.C., 1983. Earthquakes in the Orozco Transform Zone: seismicity, source mechanisms, and tectonics. J. Geophys. Res. Solid Earth 88, 8203–8225. https://doi.org/10.1029/JB088iB10p08203.
Tsai, V.C., Nettles, M., Ekström, G., Dziewonski, A.M., 2005. Multiple CMT source analysis of the 2004 Sumatra earthquake. Geophys. Res. Lett. 32 https://doi.org/10.1029/2005GL023813.
Utsu, T., 1966. A statistical significance test of the difference in *b*-value between two earthquake groups. J. Phys. Earth 14, 37–40. https://doi.org/10.4294/jpe1952.14.37.
Utsu, T., 1999. Representation and analysis of the earthquake size distribution: A historical review and some new approaches. Pure Appl. Geophys. 155, 509–535.
Uyeda, S., Kanamori, H., 1979. Back-arc opening and the mode of subduction. J. Geophys. Res. Solid Earth 84, 1049–1061. https://doi.org/10.1029/JB084iB03p01049.
Wadati, K., 1928. On shallow and deep earthquakes. Geophys. Mag. 1, 162–202.
Wadati, K., 1934. On the activity of deep focus earthquakes and in the Japan Island and neighbourhoods. Geophys. Mag. 8, 305–325.
Ward, S.N., 1994. A multidisciplinary approach to seismic hazard in southern California. Bull. Seismol. Soc. Am. 84, 1293–1309.
Wei, S.S., Wiens, D.A., van Keken, P.E., Cai, C., 2017. Slab temperature controls on the Tonga double seismic zone and slab mantle dehydration. Sci. Adv. 3 (1), e1601755. https://doi.org/10.1126/sciadv.1601755 (9 pp.).
Weston, J., Engdahl, E.R., Harris, J., Di Giacomo, D., Storchak, D.A., 2018. ISC-EHB: reconstruction of a robust earthquake data set. Geophys. J. Int. 214, 474–484. https://doi.org/10.1093/gji/ggy155.
Wiens, D.A., Stein, S., 1984. Intraplate seismicity and stresses in young oceanic lithosphere. J. Geophys. Res. Solid Earth 89, 11442–11464. https://doi.org/10.1029/JB089iB13p11442.
Wiens, D.A., McGuire, J.J., Shore, P.J., Bevis, M.G., Draunidalo, K., Prasad, G., Helu, S.P., 1994. A deep earthquake aftershock sequence and implications for the rupture mechanism of deep earthquakes. Nature 372, 540–543. https://doi.org/10.1038/372540a0.
Wilcock, W.S.D., Purdy, G.M., Solomon, S.C., DuBois, D.L., Toomey, D.R., 1992. Microearthquakes on and near the East Pacific Rise, 9°–10°N. Geophys. Res. Lett. 19, 2131–2134. https://doi.org/10.1029/92GL02208.
Wysession, M.E., Okal, E.A., Miller, K.L., 1991. Intraplate seismicity of the Pacific Basin, 1913–1988. Pure Appl. Geophys. 135, 261–359. https://doi.org/10.1007/BF00880241.
Yoshioka, S., Daessler, R., Yuen, D.A., 1997. Stress fields associated with metastable phase transitions in descending slabs and deep-focus earthquakes. Phys. Earth Planet. Inter. 104, 345–361. https://doi.org/10.1016/S0031-9201(97)00031-9.
Zhan, Z., 2017. Gutenberg–Richter law for deep earthquakes revisited: a dual-mechanism hypothesis. Earth Planet. Sci. Lett. 461, 1–7. https://doi.org/10.1016/j.epsl.2016.12.030.
Zhan, Z., 2020. Mechanisms and implications of deep earthquakes. Annu. Rev. Earth Planet. Sci. 48, 147–174. https://doi.org/10.1146/annurev-earth-053018-060314.